Combustion and Flame 161 (2014) 866–884

Contents lists available at ScienceDirect

Combustion and Flame

journal homepage: www.elsevier.com/locate/combustflame

A chemical mechanism for low to high temperature oxidation of *n*-dodecane as a component of transportation fuel surrogates

Krithika Narayanaswamy [a,*], Perrine Pepiot [b], Heinz Pitsch [a,c]

[a] *Department of Mechanical Engineering, Stanford University, CA 94305, United States*
[b] *Sibley School of Mechanical and Aerospace Engineering, Cornell University, NY 14853, United States*
[c] *Institute for Combustion Technology (ITV), RWTH Aachen University, Templergraben 55, 52056 Aachen, Germany*

ARTICLE INFO

Article history:
Received 23 June 2013
Received in revised form 5 September 2013
Accepted 12 October 2013
Available online 15 November 2013

Keywords:
Chemical mechanism
Kinetics
Normal alkanes
Fuel surrogates
n-Dodecane

ABSTRACT

Using surrogate fuels in lieu of real fuels is an appealing concept for combustion studies. A major limitation however, is the capability to design compact and reliable kinetic models that capture all the specificities of the simpler, but still multi-component surrogates. This task is further complicated by the fairly large nature of the hydrocarbons commonly considered as potential surrogate components, since they typically result in large detailed reaction schemes. Towards addressing this challenge, the present work proposes a single, compact, and reliable chemical mechanism, that can accurately describe the oxidation of a wide range of fuels, which are important components of surrogate fuels. A well-characterized mechanism appropriate for the oxidation of smaller hydrocarbon species [G. Blanquart, P. Pepiot-Desjardins, H. Pitsch, Chemical mechanism for high temperature combustion of engine relevant fuels with emphasis on soot precursors, Combust. Flame 156 (2009) 588–607], and several substituted aromatic species [K. Narayanaswamy, G. Blanquart, H. Pitsch, A consistent chemical mechanism for the oxidation of substituted aromatic species, Combust. Flame 157 (10) (2010) 1879–1898], ideally suited as a base to model surrogates, has now been extended to describe the oxidation of *n*-dodecane, a representative of the paraffin class, which is often used in diesel and jet fuel surrogates. To ensure compactness of the kinetic scheme, a short mechanism for the low to high temperature oxidation of *n*-dodecane is extracted from the detailed scheme of Sarathy et al. [S. M. Sarathy, C. K.Westbrook, M. Mehl, W. J. Pitz, C. Togbe, P. Dagaut, H. Wang, M. A. Oehlschlaeger, U. Niemann, K. Seshadri, Comprehensive chemical kinetic modeling of the oxidation of 2-methylalkanes from C_7 to C_{20}, Combust. Flame 158 (12) (2011) 2338–2357] and integrated in a systematic way into the base model. Rate changes based on recent rate recommendations from literature are introduced to the resulting chemical mechanism in a consistent manner, which improve the model predictions. Extensive validation of the revised kinetic model is performed using a wide range of experimental conditions and data sets.

1. Introduction

Computational combustion studies in engines typically use surrogates to model real fuels. However, it is challenging to develop kinetic models that describe the oxidation of all individual components in multi-component surrogates accurately. Further, the nature of the hydrocarbons commonly considered as surrogate components often leads to extremely large reaction schemes for surrogate mixtures, owing to the large detailed reaction schemes for the individual component description. As a result, designing compact kinetic models is yet another formidable task. It is our objective to meet these challenges, by developing a single, consistent, reliable, and compact chemical mechanism, that can describe the oxidation of essential components of transportation fuel surrogates, and the present work makes a contribution towards achieving this goal.

In a recent work, a single chemical mechanism describing the oxidation of a wide range of hydrocarbon species, from C_1 to C_8 species was proposed and validated extensively against experimental data for the oxidation of several compounds [1], with emphasis on detailed soot modeling and surrogate fuel formulations. In addition to smaller hydrocarbons, which are well considered in that model, jet fuels consist of up to 16–18% of aromatic compounds [2,3], and these play a crucial role in soot formation. Accordingly, the mechanism was extended in a consistent manner to describe the moderate to high temperature oxidation of several aromatics, viz. toluene, ethylbenzene, styrene, *m*-xylene, and α-methylnaphthalene [4]. The resulting scheme was validated thoroughly against available experimental data for the substituted

---

* Corresponding author.
E-mail address: krit87@stanford.edu (K. Narayanaswamy).

0010-2180/$ - see front matter © 2013 The Combustion Institute. Published by Elsevier Inc. All rights reserved.
http://dx.doi.org/10.1016/j.combustflame.2013.10.012

aromatics under consideration. The purpose of this work is to extend this mechanism, ideally suited as a base to model surrogate blends, to include the low to high temperature oxidation pathways of a representative of the paraffin class, important in engine fuels.

Longer chain alkanes, such as *n*-decane, *n*-dodecane, and *n*-tetradecane, are potential candidates to represent the paraffin class in transportation fuel surrogates. Out of these normal alkanes, *n*-dodecane could be interesting as a surrogate component [5,6], and has been identified as a good compromise between a longer straight chain alkane, typical for transportation fuels, and a reasonable size of the molecule [7]. Following this, *n*-dodecane is chosen as the paraffin representative for this work.

Few detailed mechanisms for *n*-dodecane exist in the literature. A detailed reaction scheme to describe the pyrolysis of *n*-dodecane was developed by Dahm et al. [8], and later improved and extended by Herbinet et al. [9]. Their improved model was used to predict the results of pyrolysis experiments and thermal decomposition in a jet-stirred reactor at low to moderate temperatures (773–1073 K). Biet et al. [10] suggested improvements to the rate rules used in the EXGAS software for better modeling of low temperature oxidation of large linear alkanes ($>C_{10}$). They proposed a semi-detailed kinetic model applicable at low through intermediate temperatures (550–1100 K), and modeled pressurized flow reactor data for *n*-dodecane using their kinetic model. Ranzi et al. [11] proposed a lumped mechanism for *n*-alkanes including *n*-dodecane for low to high temperature oxidation and validated their model against pressurized flow reactor data and in counter flow flame configurations. Recently, a detailed kinetic scheme to describe the low to high temperature kinetics of *n*-undecane and *n*-dodecane was developed by Mzé-Ahmed et al. [12]. The proposed scheme was validated against their jet stirred reactor data for *n*-dodecane, and their model predictions have been compared against ignition delays and species profile measurements for *n*-dodecane.

Of particular interest to this work are the chemical models for alkane oxidation developed by the kinetics group at Lawrence Livermore National Laboratories (LLNL). Westbrook et al. [13] proposed a detailed kinetic scheme to describe the pyrolysis and oxidation of several *n*-alkanes up to *n*-hexadecane. This reaction mechanism includes high and low temperature oxidation pathways. Sarathy et al. [14] improved this detailed model for normal alkanes, further extending it to methyl alkanes from C_8 to C_{20}. Specifically, the C_0–C_5 sub-mechanism was updated based on Healy et al. [15], and new reaction pathways such as the concerted elimination pathway to form alkene and HO_2 from the alkyl peroxy radical were introduced to the normal alkane chemistry. The reaction rates for H-abstraction from alkenes were updated, and the activation energies for alkenyl decompositions were modified. These reaction schemes are built in a modular approach, based on well-established reaction classes, and associated rate rules originally developed for *n*-heptane by Curran et al. [16,17], and further updated as per the Mehl et al. mechanism [18] for gasoline surrogate.

Considering moderate and high temperature oxidation, You et al. [19] proposed a kinetic model for normal alkanes up to *n*-dodecane applicable above 850 K. The reaction mechanism includes the high temperature pyrolysis and oxidation of normal alkanes (C_5–C_{12}), and a global 4-species, 12-step reaction set appended to this captures some of the intermediate temperature chemistry. They validated their kinetic model against fuel pyrolysis in plug flow and jet-stirred reactors, laminar flame speeds, and ignition delays behind reflected shock waves, with *n*-dodecane being the emphasis. This reaction scheme forms the basis for the *n*-dodecane sub-mechanism in JetSurF [20], which is an ongoing effort towards a jet fuel surrogate mechanism. The JetSurF mechanism includes some revisions to the previous You et al. model, and has been tested more widely against experimental data at moderate to high temperatures.

In summary, among the several reaction mechanisms that have been proposed for *n*-dodecane oxidation, these models [10–14] have the capability to describe low through high temperature chemistry, which is of interest to this work. It should also be noted that the relevance of *n*-dodecane as a component of jet fuel surrogates has attracted a number of experimental studies in the last couple of years, thus widening the experimental database on *n*-dodecane oxidation [12,21–29]. A vast majority of these experimental data were obtained after the development of the above mentioned kinetic models, and in some cases, those reaction mechanisms were not validated against all existing data, for example, species profile measurements. There is therefore a rich experimental database that is yet to be fully utilized for model evaluation and improvement.

The prime objective of the present work is to (i) leverage this recent experimental knowledge to develop and extensively validate a model for low through high temperature oxidation of *n*-dodecane, (ii) ensure that the proposed reaction scheme retains a compact size, which is amenable to comprehensive kinetic analysis, and (iii) progress towards a single chemical mechanism that can accurately describe the oxidation of a wide range of fuels, which are important surrogate components. The present model is built as an additional module on an existing well-validated model, whose base chemistry has been treated consistently [1,4], and thereby ensures kinetic compatibility between the various individual components included in the multi-component scheme by construction. Also, great care is taken to ensure that the oxidation of *n*-heptane, iso-octane, and aromatics, well described in this base model, is little impacted by the introduction of the *n*-dodecane model.

In extending the base model of Ref. [4] to include the low through high temperature oxidation pathways of *n*-dodecane, it is desired to introduce only the necessary kinetics to ensure the compactness of the model. Therefore, in the present approach, mechanism reduction techniques developed previously by Pepiot and Pitsch [30,31] are employed to first obtain a reduced reaction scheme applicable to low through high temperature oxidation of *n*-dodecane from a reference mechanism, which is then incorporated into the base model. In this reduction technique, each reduction step, *i.e.* elimination of species, elimination of additional reactions, and lumping, is performed in one sweep with a single evaluation of source terms at the considered conditions. This technique therefore avoids reduction by cancelation of errors by only neglecting species and reactions that have truly a small influence on the reaction fluxes. Since the chemical mechanisms being combined are small in size, the risk of introducing truncated paths or involuntarily duplicating reaction pathways in the combined mechanism is best circumvented by this approach.

Considering the choice of the reference mechanism, while much effort has gone into developing the JetSurF [20] model that describes the oxidation of *n*-dodecane, since low temperature chemistry is also of interest here, for consistency, it is found best to start with a reaction mechanism that already includes these pathways. The recent detailed reaction scheme proposed by Sarathy et al. [14] is chosen as the reference mechanism for the present work. This kinetic scheme describes the low through high temperature chemistry of normal alkanes (including *n*-dodecane) and is constructed from elementary reactions, which is more consistent with our base model and the aforementioned mechanism reduction approach than the Biet et al. [10] and Ranzi et al. [11] models, which are semi-lumped in nature. The reaction mechanism of Sarathy et al. [14] also takes into account the recent knowledge on newer reaction pathways, for instance, the concerted elimination pathway, as well as a better description of auto-ignition, compared to the Mzé-Ahmed et al. [12] model.

Note that the reduction techniques referred above involve chemical lumping of isomer species, which contributes significantly to the reduction in model size. Therefore, the incremental *n*-dodecane module added to the base model involves reactions among some lumped species as well. This imposes certain restrictions on the modifications of reaction rate data that could be introduced in this combined reaction mechanism. For instance, it is not possible as such to introduce rate changes for reactions involving single isomer species that exist as lumped species in the combined model. However, owing to the large size of the reference mechanism, the alternative approach of combining the reference *n*-dodecane mechanism with the base model, and then introducing rate changes and validating the combined model, followed by model reduction is nearly impossible. The huge size of the combined mechanism prior to model reduction discourages reaction flux analysis and sensitivity studies, which are often used to identify deficiencies in the reaction mechanism, such as missing pathways and incorrect reaction rates, thereby pointing to changes required to improve the description of the underlying kinetics.

The approach adopted in this work wins on this front, and has the advantages of simplicity, by minimizing the kinetic incompatibilities required to be dealt with when merging kinetic modules from different sources, and assures a quick turn around time to arrive at a reliable chemical model. In the event that an elementary reaction rate needs to be updated for a single isomer species that exists as a lumped species in the combined model, the rate change could be introduced in the reference mechanism, the automatic reduction procedure could be repeated easily, and the revised reduced mechanism combined with the base model to give the final updated model in a short time.

The methodology involved in arriving at a reduced skeletal level model from the reference *n*-dodecane mechanism is described in Section 2.1. This is followed by a discussion on incorporating the reaction pathways in the condensed scheme into the base model in Section 2.2. A few reaction rate changes are introduced to the combined model based on recent theoretical and experimental studies, and these help achieve improved model predictions. These changes, described in Section 2.3, have been consistently incorporated by treating all C_4–C_{12} alkane derivatives in a similar manner. A demonstration of the performance of the revised reaction model for different targets follows in Section 3. The article is then concluded by summarizing the capabilities of this model in describing low through high temperature oxidation of *n*-dodecane.

2. Mechanism development

2.1. Skeletal mechanism for n-dodecane

The detailed mechanism for *n*-dodecane oxidation from Sarathy et al. [14], chosen here as the reference model, and referred to below as the LLNL mechanism, has tens of thousands of reactions among ~1480 species, not counting the sub-mechanisms for the larger alkanes (C_{13}–C_{16}) and the 2-methyl alkanes (C_8–C_{20}), which are also described in the reference model. First, this extensive mechanism is reduced to a skeletal level using a multi-stage reduction strategy put forth by Pepiot and Pitsch, involving automatic species and reaction elimination using the DRGEP approach [30], and chemical lumping of species [31]. The database used to carry out the reduction includes homogeneous, adiabatic, isobaric and isochoric reactor configurations at low to high temperatures (T = 600–1500 K), pressures ranging from P = 1–40 atm, and equivalence ratios spanning lean to rich conditions (ϕ = 0.5–1.5). The concentrations of fuel, oxidizer, and major combustion products, and ignition delays, where the ignition time is determined by locating the time instant of steepest rise in simulated temperature profile and extrapolating back in time to the pre-ignition baseline, are used as targets in the reduction process.

The reduced reaction mechanism obtained after performing species and reaction elimination on the reference mechanism consists of 294 species and 1365 reactions. Lumping isomer species into a smaller number of representative species is essential to obtain compact schemes for large alkane oxidation. The choice of isomers to be lumped together was found to be crucial to correctly reproduce the ignition delay times at $T < 1000$ K. As proposed by Ahmed et al. [32], and used in Pepiot and Pitsch [31], the isomers of species important at these lower temperatures have been grouped here according to the size of the ring involved in the transition state of the corresponding isomerization reactions. For instance, the hydroperoxy dodecyl radical isomers ($C_{12}H_{24}OOH$) involving 5-member, 6-member, and 7-member ring transition states are grouped separately. A similar grouping was extended to other species important at lower temperatures, namely the cyclic ether isomers ($C_{12}H_{24}O$), peroxy hydroperoxy dodecyl isomers ($O_2C_{12}H_{24}OOH$), and the ketohydroperoxide ($C_{12}KET$) isomers.

While large isomers usually have similar production and consumption routes (thus justifying lumping these isomers together), this is not the case for smaller molecules, and lumping these is not justified chemically. Therefore, isomers of smaller species ($<C_4$) have been retained as individual species in this work. Also, those isomers in the detailed model that exist as individual species in the base model are not lumped to ensure kinetic compatibility between the two models. Upon chemical isomer lumping, a reduced reaction mechanism consisting of 188 species and 1025 reactions is obtained. With a further step of species and reaction elimination performed on this reaction mechanism, the final skeletal level mechanism is obtained.

The skeletal mechanism for *n*-dodecane thus obtained consists of 876 reactions among 164 species. The reduction procedure provides an accurate skeletal level model, the maximum error in ignition delays being ~18% at the lowest temperature point considered, with an average error of ~5%, the time integrated error in major species concentrations being <4%, and the maximum error in final concentrations being ~8%, compared to the reference detailed mechanism. In Fig. 1(a), a comparison between the ignition delays computed using the detailed and skeletal schemes for lean, stoichiometric, and rich *n*-dodecane/air mixtures at P = 20 atm shows very good agreement over the entire temperature range, spanning low through high temperatures. The skeletal mechanism also reproduces the OH time histories obtained using the detailed reaction mechanism in Fig. 1(b). Further, the laminar flame speeds computed using the reduced mechanisms at different stages of reduction in Fig. 1(c) show a good agreement (a maximum difference of 4% at lean conditions), thereby demonstrating the high accuracy retained throughout the reduction procedure.

A high reduction in size (~90%) is achieved in the skeletal level mechanism with small errors in ignition delays, species time histories, laminar flame speeds (see Fig. 1), and concentration profiles in flow reactor configurations (not shown here) compared to the detailed kinetic mechanism. This skeletal scheme is used in the subsequent mechanism development steps.

2.2. Combined mechanism

The merging of the skeletal level *n*-dodecane model with the base model is accomplished using an interactive tool [33] that automatically identifies common species and reactions from the different mechanisms, and incompatibilities between the kinetic data sets. The resulting combined mechanism includes the oxidation pathways of *n*-dodecane at low through high temperatures in addition to several hydrocarbons already described in the base mechanism. The additional reaction set also includes the low and intermediate temperature chemistry of C_1–C_4 species, which was absent in the base model, since the base model chemistry was

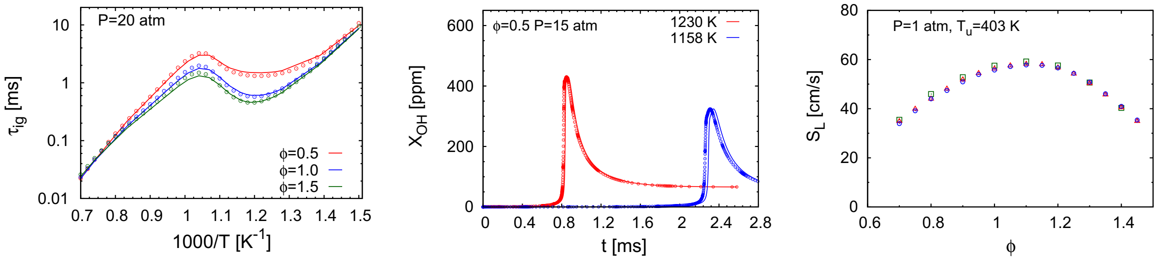

(a) Ignition delay times (b) OH time history (c) Laminar flame speeds

Fig. 1. Comparing (a) ignition delay times of *n*-dodecane/air mixtures and (b) OH time history during *n*-dodecane/O_2/Ar oxidation between the detailed model of Sarathy et al. [14] [LLNL] (lines) and the skeletal model (○) derived in the present work, (c) laminar flame speeds simulated using reaction mechanisms obtained at different stages of reduction: (i) a reference, slightly reduced mechanism obtained from species elimination as described in Section 2.1, with very strict error tolerances (<0.1%) compared to the detailed mechanism, comprising of 587 species and 4903 reactions (□), (ii) the reduced model prior to the lumping stage of reduction, consisting of 294 species and 1365 reactions (△), and (iii) the skeletal model (○). The skeletal model refers to the final reduced scheme obtained from the detailed model of Sarathy et al., prior to combining with the base model.

mainly developed to address high temperature oxidation. These include reactions of species: $HOCH_2O$, OCHO, HOCHO, O_2CHO, HO_2CHO, CH_3CO_3, CH_3CO_2, CH_3OCO, CH_3CO_3H, and CH_3COCH_2, to mention a few.

The incremental *n*-dodecane module consists of 496 reactions among 96 species. A sketch of the main oxidation pathways of the fuel (*n*-dodecane) and its C_{12} derivatives in this incremental reaction set is outlined in Fig. 2. The reaction pathways of *n*-dodecane belonging to the different reaction classes identified as important for the low through high temperature oxidation of normal alkanes in the detailed mechanism, are retained in this combined model. Note that the dodecyl radicals, peroxy, and hydroperoxy dodecyl species are present as lumped species in this reaction set. In contrast to this, for the smaller C_5–C_{11} alkyl derivatives, the reduction procedure retains only the most important isomer species in this incremental reaction set. These include the corresponding 1-alkene, the lumped alkenyl radical (also appearing as a lumped species in the detailed mechanism), the 1-peroxy radical, the 1-3-hydroperoxy alkyl radical (6-member ring in the transition state, $C_nH_{2n}OOH$), the 1-3-peroxy hydroperoxy alkyl radical, and the 1-3-ketohydroperoxide. The 1-3-hydroperoxy alkyl derivatives of all C_5–C_{11} alkanes form OH, CH_2O, and the corresponding smaller 1-alkene as

$$1\text{-}3C_nH_{2n}OOH \rightarrow OH + CH_2O + C_{n-1}H_{2n-2}. \qquad (1)$$

The cyclic ether formation reactions from these smaller carbon hydroperoxy alkyl species were discarded during the model reduction step.

The steps below have been followed to insure a smooth and consistent merging. Rate conflicts detected during the merging were always resolved in favor of the thoroughly validated base model, therefore leaving this mechanism virtually unchanged. Duplicate reaction pathways in the combined model coming from the incremental dodecane reaction scheme were identified and removed appropriately. Finally, the validation tests for the substituted aromatics presented in our earlier work [4] were repeated using the combined mechanism, and only minor changes were observed in the model predictions.

Figure 3 compares the ignition delay time predictions using the detailed model, the skeletal level model, and the combined model at $\phi = 1.0$ and $P = 20$ atm. As discussed previously, the skeletal mechanism retains the same level of accuracy for ignition delay predictions as the detailed mechanism. The combined model closely follows the ignition delay time predictions of the skeletal model at temperatures $T < 1100$ K. At higher temperatures, the combined model predicts shorter ignition delays owing to the difference in the C_1–C_4 high temperature chemistry between the skeletal model and the base model.

2.2.1. Need for an improved model

Ignition delays at low through high temperatures, and species profiles measured in shock tube experiments are two of the targets

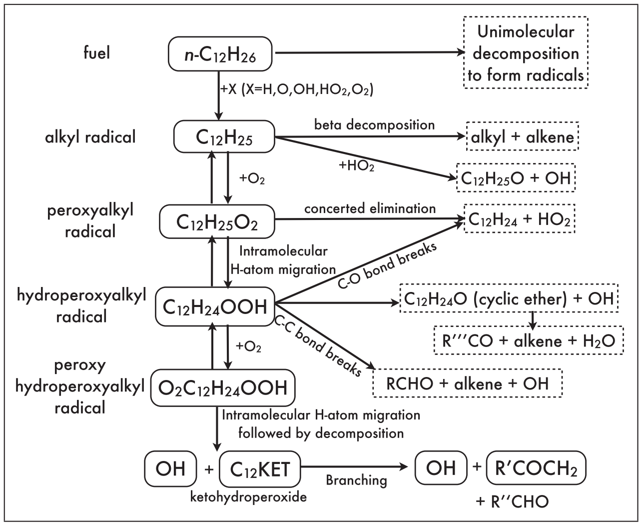

Fig. 2. Main oxidation pathways of *n*-dodecane and its C_{12} derivatives in the combined model, which is the reaction mechanism obtained by merging the skeletal level *n*-dodecane mechanism with the base model (see text for details). The reaction pathways present in the detailed model, that are important for the low through high temperature oxidation of *n*-dodecane, are retained here.

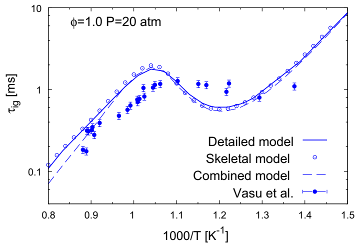

Fig. 3. Comparing ignition delays of stoichiometric *n*-dodecane/air mixtures at $P = 20$ atm computed using the (i) detailed mechanism of Sarathy et al. [14] (—), (ii) skeletal model (○), obtained by reducing the detailed Sarathy et al. model, and (iii) combined model (---), obtained by merging the skeletal model with the base model [4], against the experimental data from Vasu et al. [21] (filled symbols). Ignition delays of *n*-dodecane are determined in the experiments [21] by locating the time of steepest rise in pressure and linearly extrapolating back in time to the pre-ignition baseline (overall uncertainty of ±10%), and the simulations follow the same ignition criteria. The differences observed between the combined model results and the measurements, call for revisions to the kinetic scheme.

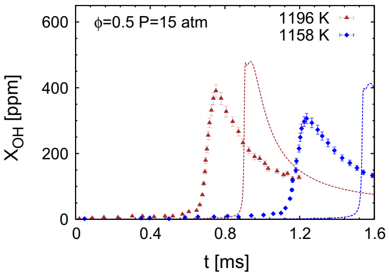

Fig. 4. Comparing OH time histories during the oxidation of *n*-dodecane/O_2/argon mixtures at $P = 15$ atm, $\phi = 0.5$ between the combined model (lines) with experimental data from Vasu et al. [21] (symbols). The time at which the OH profile rises is delayed in the computations, pointing to the need for improving the underlying kinetics.

that the model should be able to predict. The ignition delays of stoichiometric *n*-dodecane/air mixtures measured by Vasu et al. [21] at pressures, $P = 18$–28 atm, have been scaled to $P = 20$ atm, according to P^{-1} scaling law adopted in their work, and plotted in Fig. 3. Comparing the ignition delays from the skeletal model and the combined model in conjunction with the experimental data, one could argue that the shorter ignition delays predicted by the combined model at higher temperatures ($T > 1100$ K) are closer to the experimental ignition delays at these temperatures, even though the agreement is far from satisfactory. However, at temperatures $T < 1100$ K ($1000/T > 0.9$ K^{-1}), the skeletal model, and therefore the combined model, capture neither the slope of the ignition delay times in the Negative Temperature Coefficient (NTC) region, nor the magnitudes of the ignition delays. The ignition delay time predictions need to be improved: predicted ignition delays should be shorter at higher temperatures ($T > 1000$ K), and longer in the NTC region, to obtain better agreement with experimental measurements.

Vasu et al. [21] also measured OH time histories during the oxidation of *n*-dodecane/O_2/argon mixtures at a pressure of $P = 15$ atm and $\phi = 0.5$. The OH profiles computed using the combined model are compared with this experimental data set at two different temperatures in Fig. 4. The peak values of OH concentrations are over-predicted by about 20%, and the time at which the OH profile rises is delayed in the computations, albeit an earlier rise compared to the skeletal mechanism predictions (see OH profiles at $T = 1158$ K in Fig. 1(b)). This again calls for improvements to the underlying reaction model.

Starting from the combined model described above, which will be called *CPM* model (for combined, prior to modifications) in the following, a small number of reaction rate changes have been introduced to improve the predictive capability of the model and to simply update the model to more recent kinetic rate data. These updates are guided by sensitivity studies, and the following subsection discusses these in detail. Note that the sensitivity study is itself greatly facilitated and the rate changes are easy to incorporate in the combined model owing to the now compact set of *n*-dodecane oxidation reactions considered. The updates to the rate parameters are primarily based on theoretical calculations and rate recommendations available in literature. The revised model results in improved predictions for the various idealized configurations.

2.3. Modifications to the reaction mechanism

2.3.1. H_2/O_2 chemistry

First, the H_2/O_2 chemistry of the underlying base model has been updated based on the recent Burke et al. [34] reaction mechanism. This change impacts the ignition delay results at $800\text{ K} < T < 1100$ K, making ignition delays longer, as seen from Fig. 5(a). The difference is predominantly due to the rate assigned to the H_2O_2 (+M) → 2 OH (+M) reaction, which is particularly important for ignition in the NTC regime of ignition. Burke et al. obtained the rate of this reaction from the recent calculations performed by Troe [35], which allows an appropriate fall off treatment for the pressure dependence of this reaction rate.

A sensitivity analysis was carried out at $P = 20$ atm, $\phi = 1.0$, and $T \sim 850$ K in the NTC ignition regime and $T \sim 1000$ K in the regime where the ignition behavior transitions into high temperature ignition, to reveal the reactions that are important for ignition delay predictions. The reactions among C_{12} derivatives that show large sensitivities at these temperatures are summarized in Fig. 6. Reactions showing positive sensitivity factors make ignition delays longer, and those showing negative sensitivity factors result in faster ignition.

2.3.2. Formation of ketohydroperoxide and OH

The significance of peroxy hydroperoxy dodecyl radical ($O_2C_{12}H_{24}OOH$) forming ketohydroperoxide and OH for ignition delay predictions in the NTC ignition regime can be seen from Fig. 6(a) (fourth highest sensitivity factor). The rates of the analogous reactions for smaller alkane derivatives,

$$C_nH_{2n}OOH1\text{-}3O_2 \rightarrow C_nKET1\text{-}3 + OH, \tag{2}$$

where $4 < n < 11$, also have an impact on the ignition delays at these moderate temperatures. The slower these reaction rates, the longer the ignition delays will be in the NTC region. Note that these smaller carbon derivatives ($<C_{12}$) exist as individual species in the incremental *n*-dodecane reaction set. The above reaction (2) involves the migration of an H atom bound to the primary carbon (attached to the –OOH group) in $C_nH_{2n}OOH1\text{-}3O_2$, to the peroxy radical site on the carbon third from the terminal carbon: in short, a 1-5p H-migration. This is followed by a release of an OH radical, and the ketohydroperoxide formation, which is considered to be a fast process.

The detailed model of Sarathy et al. [14] treats the ketohydroperoxide formation reactions similarly to the corresponding peroxy alkyl isomerization reactions,

$$C_nH_{2n+1}O_2\text{-}3 \leftrightarrow C_nH_{2n}OOH3\text{-}1. \tag{3}$$

They assign the rate constant of reaction (3) to reaction (2), with the pre-exponential factor modified to account for the number of H atoms available for migration, and with the activation energy reduced by 3 kcal/mol, to account for the weakened C–H bond in the peroxy hydroperoxy alkyl radical owing to the presence of the –OOH group. While this reduction in activation energy, which allows the intramolecular H-migration in the case of reaction (2) to take place faster than that for reaction (3), is agreeable, the magnitude of the reduction has been revisited in the present work. Sharma et al. [36] considered intramolecular H-migration reactions of RO_2 and O_2QOOH radicals for small carbon systems in their quantum chemical calculations. In particular, they found the activation energy for 1-5p H-migration in $CH_3CH(OO)CH_2CH_2OOH$ to be 0.9 kcal/mol less than that for $CH_3CH(OO)CH_2CH_3$. In accordance with this study, in the present work, the activation energies for reaction (2), which involve a 1-5p H-migration, have been reduced from their corresponding peroxy radical isomerization reactions by 0.9 kcal/mol consistently for all such reactions involving smaller carbons in the range of C_5–C_{10}. Note that this does not warrant a change to the corresponding C_{12} reaction rates, since the secondary H atom migrations dominate the C_{12} chemistry.

Sharma et al. [36] have also considered the migration of a secondary H atom involving a 6-membered ring transition state, *i.e.* a 1-5s migration, in RO_2 and O_2QOOH radicals. According to their study, the activation energy of 1-5s H-migration in peroxy hydroperoxy pentyl radical is found to be 1 kcal/mol lower than that for the corresponding peroxy radical. However, from the calculations

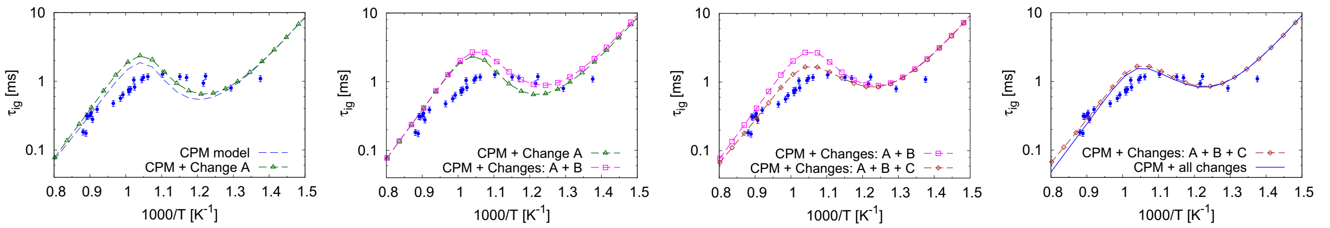

(a) Effect of Change A (b) Effect of Change B (c) Effect of Change C (d) Effect of Changes D, E, and F

Fig. 5. Effect of different changes introduced to the CPM model on the ignition delays of stoichiometric *n*-dodecane/air mixtures at $P = 20$ atm; symbols – experiments of Vasu et al. [21] (●); lines – simulations using reaction mechanisms at different stages of updates to the CPM model. Description of changes: (A) – updated H_2/O_2 chemistry from Burke et al. [34], (B) – rate of formation of ketohydroperoxide and OH, (C) – rate of H-abstraction by HO_2 from *n*-dodecane, (D, E, F) – Alkene/Alkenyl decomposition and H-abstraction rates. The results obtained using the updated reaction mechanism (—), same as the "CPM + all changes" model, show an improved agreement with the experimental data compared to the CPM model (---) at all temperatures.

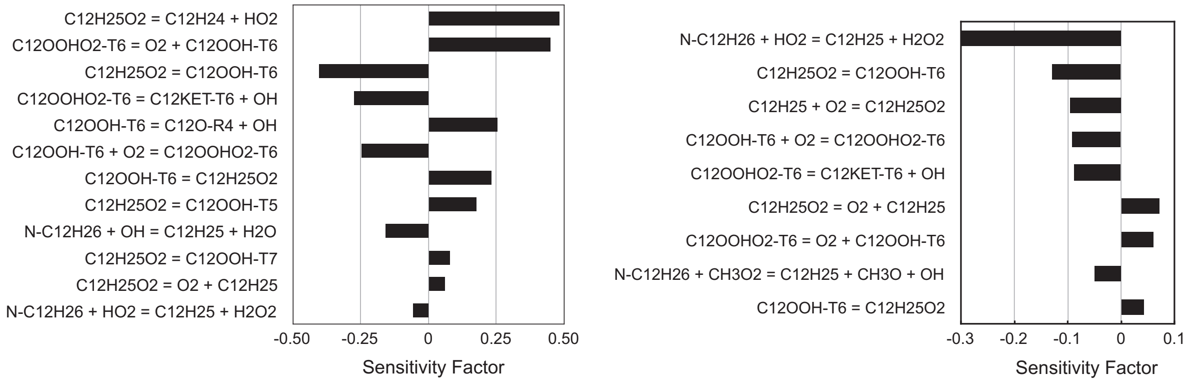

(a) $T = 850\,\text{K}$ (b) $T = 1000\,\text{K}$

Fig. 6. Sensitivity analysis for ignition delays of *n*-dodecane/air mixtures at $\phi = 1.0$ and $P = 20$ atm using the CPM model (combined, prior to modifications model). Sensitivities are determined by multiplying each rate constant by a factor of 2, and finding the change in ignition delays due to the rate change. Only reactions among C_{12} derivative species with sensitivity factor >5% are reported here. Refer to Supporting materials (Tables S1–S3) for a description of the generic names used for the lumped C_{12} species in this figure.

of Asatryan and Bozzelli [37] at the same level of theory as Sharma et al. and a recent study by Cord et al. [38], this difference in energies could be derived as 4 kcal/mol and 2.7 kcal/mol respectively. Considering that the reduction in E_{act} used in the reference Sarathy et al. [14] model for 1-5s migration in RO_2 and O_2QOOH radicals, equal to 3 kcal/mol, falls within the variability of the calculations reported in Refs. [37,38], this reaction rate has not been modified in the present work.

2.3.3. H-abstraction from n-dodecane by HO_2

The changes mentioned above bring the ignition delays at $750\,\text{K} < T < 900\,\text{K}$ closer to the experimental data (see Fig. 5(b)). However, faster ignition is still required at the temperatures where the transition from the NTC to the high temperature ignition regime takes place. The sensitivity analysis at $T \sim 1000\,\text{K}$ in Fig. 6(b) particularly reveals that the rate of H-abstraction from the fuel by HO_2 is key in determining ignition delays around 1000 K:

$$n\text{-}C_{12}H_{26} + HO_2 \rightarrow C_{12}H_{25} + H_2O_2. \quad (4)$$

HO_2 behaves as a relatively stable species in the NTC region, showing little reactivity, and therefore, ignition delays at these temperatures show mild sensitivity to the above reaction rate, as seen in Fig. 6(a). However at higher temperatures, the formation of H_2O_2, and the subsequent production of OH radicals is responsible for the transition to the high temperature ignition regime.

The importance of additional pathways producing or consuming HO_2 has been examined. Alkene plus HO_2 reactions were investigated and found to have negligible effect on the ignition delays at $T \sim 1000$ K. The reaction of H-abstraction by oxygen molecule from dodecyl radical,

$$C_{12}H_{25} + O_2 \rightarrow C_{12}H_{24} + HO_2, \quad (5)$$

was also explored. This reaction class is absent in the detailed model of Sarathy et al. [14], but is now considered for all C_4–C_{12} alkyl radicals in the present model. An activation energy of 39.7 kJ/mol for reaction (5) is taken from a theoretical study of oxygen addition to *n*-butyl systems by Du et al. [39], and a pre-exponential factor of 1×10^{11} cm^3/mol s is chosen based on the rate recommended by Tsang et al. [40] for propane systems. The same reaction rate is used for all C_4–C_{12} alkyl radical reactions that belong to this reaction class. However, these reactions were found to have little influence on the ignition delays at the experimental conditions of interest here, consistent with the slow rate that Westbrook et al. [13] assigns to this reaction class. Therefore, this reaction set is not retained in the present model. Further, the reaction of dodecyl peroxy radical with HO_2, to give $C_{12}H_{25}O$, OH and O_2 was investigated, and ignition delays were found to be not very sensitive to this reaction at these temperatures. It seems therefore unlikely that the model is missing any significant consumption/production pathways involving HO_2, thus prompting a more thorough investigation of reaction (4).

While a direct evaluation of the H-abstraction rate from *n*-dodecane by HO_2 is unavailable in the literature, it can be estimated from kinetic studies available for smaller alkanes. Carstensen et al. [41] and Aguilera-Iparraguirre et al. [42] performed quantum chemistry calculations of H-abstraction reactions from *n*-butane, thus providing the reaction rates for H-abstraction by HO_2 from primary and secondary carbons in *n*-butane. Rate constants for reaction (4) can be obtained from Refs. [41,42] by scaling the *n*-butane rates to account for the number of primary and secondary carbons in *n*-dodecane, as compared to *n*-butane. These rates vary over a factor of 3–8 at different temperatures (the rate derived from Carstensen et al. being higher), attributed to the different approaches to reaction barrier computations [42]. The uncertainty associated with the calculations of Carstensen et al. is estimated to be a factor of ~4, and those of Aguilera-Iparraguirre et al. to be a factor of ~2 (estimated based on the accuracy of the reaction barriers, equal to ~4 kJ/mol [42]). For best agreement with experimental ignition delay data, a reaction rate which is 2.1 times that suggested by Aguilera-Iparraguirre et al., well within the variability of the rate constants reported (indicated above) for this reaction, is chosen here (see Fig. 5(c)). The rate of abstraction of H atom from *n*-dodecane by CH_3O_2, has also been increased by the same factor to ensure consistent treatment. Note that the original rates for these reactions in the detailed kinetic scheme of Sarathy et al. [14] were based on the Healy et al. [15] model for *n*-butane, where the H-abstraction rate by HO_2 was obtained from Aguilera-Iparraguirre et al., and the rate for H-abstraction by CH_3O_2 was obtained by reducing the rate calculated by Carstensen et al. for this reaction. Therefore, the aforementioned changes take the reaction rates closer to those prescribed by Carstensen et al. for these reactions.

It was found in the discussion above that the CPM model (combined, prior to modifications model) predicts delayed OH profile rise, which is closely related to the point of ignition, when compared to experimental concentration profiles obtained in shock tubes at high temperatures ($T > 1100$ K). Among reactions that influence the time of sharp OH rise at the experimental conditions of Vasu et al. [21], the unimolecular decomposition of alkenyl radicals into smaller radicals and alkenes is of particular interest here.

2.3.4. H-abstraction, unimolecular decomposition of alkenes

Recognizing that the H-abstraction from alkenes, mainly by H and OH, leads to the formation of the alkenyl radicals, these reactions are first considered here. The detailed model of Sarathy et al. [14] treats the abstraction reactions from larger alkenes (C_8–C_{12}) in a simplified manner, assuming the products to lead to a single lumped alkenyl radical. The reaction rates assigned are those of secondary H-abstraction from an alkane, multiplied by the number of abstractable H atoms in the alkene. However, the alkenyl radicals arising from C_6 and C_7 alkenes have been treated separately depending on the nature of the H atom abstracted, with some of the rates higher than those expected from the aforementioned rate assignment rule. In our present work, in order to ensure a consistent treatment for H-abstraction reactions from all alkenes, these reaction rates for C_6 and C_7 alkenes are treated in an analogous manner to the higher carbon alkenes. Correspondingly, the rates assigned are those of the secondary H-abstraction from an alkane, now multiplied by 12 and 14, to account for the number of abstractable H atoms in C_6H_{12} and C_7H_{14} respectively, following the rate assignment rule from Sarathy et al. [14]. The pre-exponential factor of the rate constants assigned to the H-abstraction reactions from $C_{12}H_{24}$ isomers by OH in the detailed mechanism of Sarathy et al., was found to be an order of magnitude smaller than that suggested by their rate rules for this reaction class. This reaction rate has been corrected here as per their rate rule recommendations.

Also, the rate rule for the alkene decomposition reaction to form allyl radical and a smaller alkyl radical, proposed in the detailed reaction scheme of Sarathy et al. for higher carbon alkenes (> C_7), has now been extended to C_6 and C_7 systems as well, by which an increased pre-exponential factor is assigned to these decomposition reactions. While the changes to the reaction rates of H-abstractions from alkenes resulted in little changes to the OH time histories overall, the modified alkene decomposition rates resulted in an early rise of OH profile, bringing the model predictions in better agreement with the experimentally measured profiles.

2.3.5. Unimolecular decomposition of alkenyl radicals

At high temperatures ($T > 1100$ K), the decomposition reactions of alkenyl radicals to give smaller radicals like C_2H_3, allyl (A-C_3H_5), C_4H_7, and C_5H_9, along with the formation of smaller alkenes, are important in determining the ignition delay times. For instance, the decomposition of an alkenyl radical to produce an allyl radical is given by

$$C_nH_{2n-1} \rightarrow A\text{-}C_3H_5 + C_{n-3}H_{2(n-3)}, \tag{6}$$

where $5 < n \leqslant 12$. The allyl radicals and the CH_3 radicals formed from the unimolecular decomposition of C_5H_9 radicals compete for HO_2 with the H atom according to

$$A\text{-}C_3H_5 + HO_2 \leftrightarrow C_3H_5O + OH, \tag{7}$$

$$CH_3 + HO_2 \leftrightarrow CH_3O + OH, \tag{8}$$

$$H + HO_2 \leftrightarrow OH + OH, \tag{9}$$

and thereby delay the time instant of rapid rise in OH profile. The detailed mechanism of Sarathy et al. [14] assigns an E_{act} of 25 kcal/mol for decomposition reactions leading to allyl (A-C_3H_5) radicals, while the ones leading to C_5H_9 products are assigned an E_{act} of 30 kcal/mol, and those leading to all other products are assigned an activation energy of 35 kcal/mol. The alkenyl decomposition rates leading to the formation of allyl radicals, such as in reaction (6), have been modified in the present work to the rate of C_8 H_{15} radical forming allyl and 1-pentene used in the recent Malewicki and Brezinsky [43] model, originally coming from Olchanski and Burcat [44]. The updated reaction rate has an activation energy of 30 kcal/mol, and a pre-exponential factor that is about 10 times smaller than that prescribed by Sarathy et al. for this reaction. In the present work, these rate constants have been assigned for all alkenyl decomposition reactions, irrespective of the products. This change results in a faster ignition due to an earlier OH rise at high temperatures, and better agreement with the experimentally measured OH time histories, as will be demonstrated in Section 3.2.

2.3.6. Ensuring consistency within the reaction mechanism

In the detailed model of Sarathy et al. [14], there are a few rate rules pertaining to the larger carbon systems (>C_6), which have not been applied to the smaller ones (C_4–C_6). The rate rules for these reactions: (a) the concerted elimination pathway forming HO_2 and an alkene from the peroxy alkyl radical, and (b) the decomposition of ketohydroperoxide reactions, have now been extended to the smaller carbon systems (C_4–C_6) as well. While these changes do not significantly impact the validation test results presented in this work, they have been updated in the present model to ensure that the reactions belonging to a specific reaction class are treated similarly for all carbon systems.

Figure 5(d) shows a faster ignition at higher temperatures ($T > 1100$ K) resulting from the changes to the alkenyl/alkene decomposition and H-abstraction rates. The ignition delays computed using the final revised mechanism (— in Fig. 5(d)) show an improved agreement with the experimental data compared to the CPM model (--- in Fig. 5(a)) at all temperatures.

Note that most of the changes described in this section have been introduced in the incremental *n*-dodecane reaction set, with little change to the base model, namely, the heptene and heptenyl decomposition and H-abstraction rates, which have been updated to ensure consistency, and the update to the H_2/O_2 chemistry based on Burke et al. [34]. This further re-enforces the reliability of the base model upon which the present mechanism is built. The validation tests for the potential surrogate fuel components considered in the previous works [1,4], viz. *n*-heptane, iso-octane, toluene, ethylbenzene, styrene, α-methyl naphthalene, and *m*-xylene have been repeated using the present reaction mechanism and made available with the Supporting materials (Figs. S8–S23).

This reaction mechanism, which now describes the low to high temperature oxidation of *n*-dodecane, in addition to the fuels validated in our previous works [1,4], consists of 255 species and 2289 reactions counted forward and reverse separately, among which 823 reactions are reversible. The mechanism files in chemkin and FlameMaster format can be obtained from the Supporting materials. Where listed, the forward and reverse reactions are consistent with thermodynamic data when they involve all individual (not lumped) species. When a lumped species is involved in a reaction, the reaction cannot be considered as elementary anymore. The forward and reverse rates are obtained from the lumping procedure, and are not related by the equilibrium constant of the reaction [31]. A list of the individual isomers represented by each of the lumped species present in the *n*-dodecane sub-mechanism is provided with the Supporting materials (Tables S1–S3).

The thermodynamic and transport properties for the proposed reaction mechanism have also been provided with the Supporting materials. These parameters for the base model remain the same as that provided in the previous works [1,4], with updates to the properties of species involved in H_2/O_2 chemistry based on Burke et al. [34]. For the new species added to the base model, belonging to the incremental *n*-dodecane reaction set, these properties have been obtained from that of Sarathy et al. [14]. This approach remains valid for the lumped species in the reaction mechanism as well, since only chemical isomers have been lumped together in the reduction process, which typically have similar thermodynamic and transport properties [31].

3. Validation tests

Having discussed the changes introduced to the reaction model, this section evaluates the ability of this revised mechanism to predict targets for different idealized configurations of interest, by comparing the simulated results against several experimental data sets. The validation cases focus on oxidation environments, and include (i) ignition delays spanning wide ranges of temperatures and pressures, (ii) species time histories measured in shock tubes, (iii) concentration profiles of fuel, major intermediates, and products, measured in shock tubes and pressurized flow reactors at low through high temperatures, and (iv) laminar flame speeds obtained at different pressures. In addition, species concentrations obtained in a recent pyrolysis experiment by Malewicki and Brezinsky [43] have also been considered for model evaluation, while leaving out other configurations in which kinetics is strongly coupled with diffusion, such as counterflow diffusion flame experiments, as the focus of the present work is mainly on the kinetics aspect. Table 1 summarizes the list of all experimental data relevant to *n*-dodecane, which have been considered in the present work. A few ignition delay and laminar flame speed measurements of normal alkanes, smaller than C_{12} have also been used to assess the kinetic model, by taking advantage of the similarity exhibited by the normal alkanes in these configurations.

Shock tube experiments are modeled using a constant volume homogeneous reactor configuration. Constant pressure simulations under adiabatic conditions are used to model the pressurized flow reactor experiments. Laminar flame speeds have been calculated in a manner similar to that described in Narayanaswamy et al. [4]. The simulation results discussed in this section have been computed using the present reaction mechanism, as it stands at the end of Section 2.3, unless stated otherwise. All numerical calculations have been performed using the FlameMaster code (version 3.3.9, [47]).

In addition to the test cases listed in Table 1, the simulation results have also been compared against experimental data from Refs. [8,12,48,49]. Further, mixtures of *n*-dodecane with toluene and *m*-xylene have been tested against laminar flame speeds and ignition delays. These results have been provided with the Supporting materials (Figs. S4–S7 and Figs. S24–S26) for the sake of reference.

3.1. Ignition delay times

3.1.1. High temperature ignition (above 1200 K)

The computed results are compared here against the ignition delays of lean *n*-dodecane/O_2/argon mixtures measured by Davidson et al. [23] and Vasu et al. [21], at high temperatures and different pressures. Another set of ignition delay data [24] obtained at similar conditions for stoichiometric mixtures is considered together with the corresponding species profile measurements in Section 3.2.

First, the ignition delays measured in a high pressure shock tube by Vasu et al. [21] at $P = 15$ atm, and low fuel concentrations of $X_{n-C_{12}H_{26}} = 1000$ ppm, 750 ppm, and 514 ppm, $X_{O_2} = 2$—4%, at $\phi = 0.5$, and $T = 1250$–1400 K, are discussed. Figure 7 shows the computed ignition delays in comparison to this experimental data set. To complement the small number of experimental data points for *n*-dodecane, it is of interest to consider ignition delays of other *n*-alkane/O_2/argon mixtures at comparable conditions, since these are expected to show similar ignition characteristics [13,22,50–52].

In order to make a valid comparison with other *n*-alkane ignition data, the correlation developed by Horning et al. [50] for ignition delay times of lean and stoichiometric *n*-alkane/O_2/argon mixtures can be used:

$$\tau = 9.4 \times 10^{-6} P^{-0.55} X_{O_2}^{-0.63} C^{-0.50} \exp(46550/RT), \qquad (10)$$

where ignition delay (τ) is in microseconds, pressure (P) is in atmospheres, X_{O_2} is the oxygen mole fraction, C is the number of carbons in the fuel molecule, and the activation energy is in cal/mole. This correlation was obtained from their experimental data for stoichiometric propane, *n*-butane, *n*-heptane, and *n*-decane mixtures, at $P = 1$–6 atm, $T = 1315$–1560 K, and $X_{O_2} = 2$–20%, and was found to be applicable for lean equivalence ratios and pressures up to

Table 1
List of validation cases considered in the present work for *n*-dodecane. The ignition delay and laminar flame speed measurements of normal alkanes smaller than *n*-dodecane, which have also been used to assess the kinetic model, are not listed here.

Shock tube data		Pressurized flow reactors	Burning velocity
Ignition delay and species time history	Oxidation and pyrolysis		
Vasu et al. [21] Shen et al. [22] Davidson et al. [23,24]	Malewicki and Brezinsky [43]	Kurman et al. [26] Veloo et al. [27] Hui and Sung [46]	Ji et al. [28] Kumar and Sung [45]

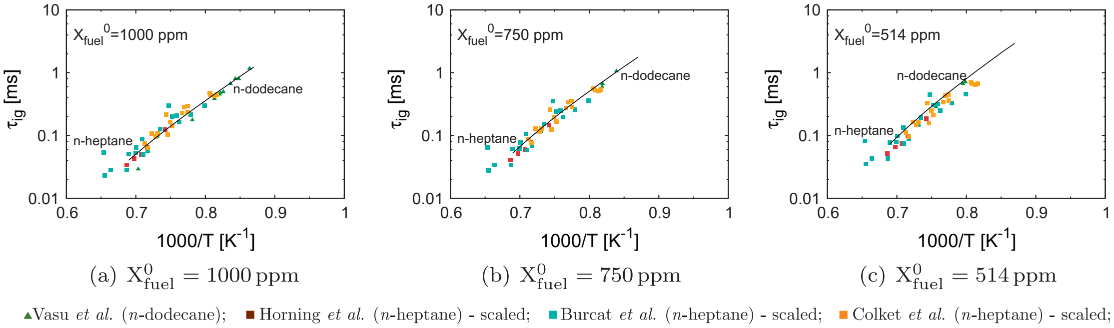

(a) $X^0_{fuel} = 1000\,\text{ppm}$ (b) $X^0_{fuel} = 750\,\text{ppm}$ (c) $X^0_{fuel} = 514\,\text{ppm}$

Fig. 7. Low fuel concentration ignition delays of fuel/O$_2$/argon mixtures at ϕ = 0.5, P = 15 atm; solid line – ignition delays of n-dodecane computed using the present reaction mechanism, where the initial n-dodecane mole fractions (X^0_{fuel}) are as indicated in the figures; symbols – experimental data for ignition delays of (i) n-dodecane [21] shown by solid triangles, and (ii) n-heptane [50,53,54] shown by solid squares. Experimental data for n-heptane/O$_2$/argon mixtures are scaled to the experimental conditions of Vasu et al. [21] using the correlation from Horning et al. [50], given by Eq. (10) (see text). These data for n-heptane are included here to complement the small number of experimental data points for n-dodecane and thereby enable a comprehensive comparison. Ignition delays of n-dodecane are defined in the experiments [21] as the time to reach 50% of the peak post-ignition X$_{OH}$ (uncertainty of ±10%), and the simulations follow the same ignition criteria.

15 atm as well. Using the correlation given by Eq. (10), the ignition delays of lean n-heptane/O$_2$/argon mixtures (ϕ = 0.5) measured by several groups [50,53,54] at different experimental conditions considered in the study of Horning et al. [50] have been scaled to the experimental conditions of Vasu et al. [21] (*i.e.* P = 15 atm and $X_{O_2} = 2$–4%), according to $P^{-0.55}$ and $X_{O_2}^{-0.63}$, and included in Fig. 7.

A comparison of the computed ignition delays with those measured by Vasu et al. [21] in Fig. 7 shows good agreement wherever data are available, except for an over-prediction at $1000/T \sim 0.7\ \text{K}^{-1}$ in Fig. 7(a). Nonetheless, when appraising the computed results together with the scaled ignition data for n-heptane, it can be concluded that the slopes of the computed ignition delays are consistent with the least square fit (not shown here) of the scaled data, for all fuel concentrations. At lower pressures, P = 6.7 atm, ignition delays of lean n-dodecane/O$_2$/argon mixtures were measured by Davidson et al. [23] in an aerosol shock tube facility, at ϕ = 0.5, and T = 1050–1330 K. In Fig. 8, the computed ignition delays of n-dodecane show good agreement with the experimental data at temperatures, $1000/T > 0.9\ \text{K}^{-1}$, although predicting faster ignition times at higher temperatures. However, following the similar lines as above, considering the simulations and the ignition delay data for n-dodecane, together with the data sets for n-heptane [50,53,54] scaled to the experimental conditions of Davidson et al. [23] (*i.e.* P = 6.7 atm and $X_{O_2} = 21\%$), using the correlation given by Eq. (10), a few comments can be made.

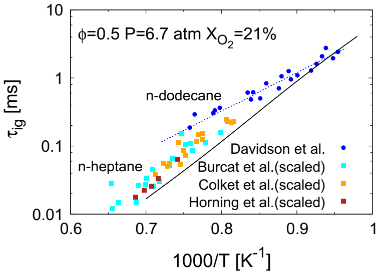

Fig. 8. Ignition delay times of fuel/O$_2$/argon mixtures at ϕ = 0.5, P = 6.7 atm; symbols – experimental data for ignition delays of (i) n-dodecane [23] (●), and (ii) n-heptane [50,53,54] (filled squares); lines – (i) ignition delays of n-dodecane computed using the present reaction mechanism (—), and (ii) fit to Davidson et al. [23] data (····). Ignition delays of n-dodecane are determined in the experiments [23] by the maximum gradient in CH emission, and the simulations follow the same ignition criteria. The n-heptane data points are scaled to the experimental conditions of Davidson et al. [23] using the correlation from Horning et al. [50], given by Eq. (10) (see text), and included here to evaluate the consistency among the different n-alkane data sets.

First, the ignition delays for n-alkanes are expected to show similar behavior and at best shorten as the size of the alkane increases [13,22,50–52], which is not true with the n-dodecane data points at temperatures where both n-alkane ignition delay measurements are available. The computed ignition delays of n-dodecane nonetheless are faster than the scaled ignition delay data of n-heptane throughout the high temperature region, in accordance with the anticipated behavior. Second, the slope of the computed ignition delays is consistent with the scaled data of n-heptane, which is not true with the n-dodecane data points (least square fit to data points shown in Fig. 8). While these factors remain, considering the uncertainties associated with the scaling law and the resulting scaled ignition delay times invoked in this discussion, it appears that further information is needed to ascertain the ability of the model to predict the ignition delays at the experimental conditions of Davidson et al. [23]. Nevertheless, from the consistency checks performed here, it can be concluded that the present model predicts the ignition delays of n-dodecane satisfactorily at high temperatures.

3.1.2. Moderate temperature ignition: 750 K < T < 1200 K

Ignition delays for n-dodecane mixtures measured by Vasu et al. [21] at P = 18–28 atm, for lean (ϕ = 0.5) and stoichiometric fuel/air ratios are considered here. Figure 9 shows a comparison of the computed ignition delays with their data scaled to P = 20 atm according to the P^{-1} scaling used in their study. The agreement between the predicted ignition delays and the experiments has improved significantly throughout the entire temperature range compared to the CPM model. The rate changes introduced in the present reaction mechanism, summarized in that section, contribute together to result in better ignition delay predictions, as shown in Fig. 5.

The faster ignition at higher temperatures (T > 1100 K) compared to the CPM model comes mainly from the changes introduced to the alkenyl decomposition reactions. The enhanced H-abstraction rate by HO$_2$ from n-dodecane is primarily responsible for the improved ignition delay predictions at 950 K < T < 1100 K. The predicted high temperature ignition delays follow the experimental data closely at ϕ = 0.5 and lie within the experimental scatter at ϕ = 1.0.

The ignition delays computed using the present reaction scheme are also able to capture the slope suggested by the experimental data in the NTC region at moderate temperatures (750 K < T < 950 K) at both lean and stoichiometric mixture conditions. The ignition delays at the lower end of this range (750–850 K) are longer compared to the CPM model, and in better

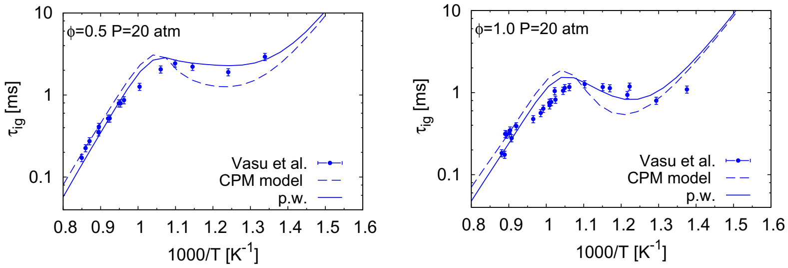

(a) $\phi = 0.5$ (b) $\phi = 1.0$

Fig. 9. Ignition delays of *n*-dodecane/air mixtures at $P = 20$ atm; lines – results obtained using the (i) present reaction mechanism (—), and (ii) CPM model (---), which is the combined model, prior to the modifications described in Section 2.3; symbols – experiments of Vasu et al. [21] (●), measured at $P = 18–28$ atm, scaled to $P = 20$ atm using P^{-1} scaling law adopted in their study. Ignition delays of *n*-dodecane are determined in the experiments [21] by locating the time of steepest rise in pressure and linearly extrapolating back in time to the pre-ignition baseline (overall uncertainty of ±10%), and the simulations follow the same ignition criteria. The combined (CPM) model results are the same as that shown in Fig. 3, and are included in this plot to highlight the improved predictions using the present model.

agreement with the experimental data due to the changes to the ketohydroperoxide formation reaction rates discussed in Section 2.3. At the higher end of this temperature range (850–950 K), the ignition delays are influenced by the rate changes introduced to the ketohydroperoxide formation and the rate of H-abstraction from the fuel by HO_2. At low temperatures, $T < 750$ K, compared to the experimental data, the simulations predicts slower ignition at $\phi = 1.0$, while reproducing the experiments at $\phi = 0.5$ satisfactorily. This will be reconsidered in conjunction with low temperature ignition data for other normal alkanes in Section 3.1.4.

Ignition delays for *n*-dodecane/air mixtures were also measured by Shen et al. [22] at $P = 12–18$ atm and $P = 38–46$ atm, and $\phi = 0.5$ and 1.0, at moderate to high temperatures. In Fig. 10, a comparison of the ignition delays between simulations and experimental data scaled according to P^{-1} used in their study, shows good agreement at temperatures ranging, $T = 1050–1250$ K, while some differences are observed in all cases at lower temperatures, with an over-prediction at 14 atm, and under-prediction at 40 atm. A point by point comparison of the ignition delays simulated at the exact pressure, temperature, and mixture conditions of Shen et al. with these experimental data in Fig. S2 also leads to the same conclusions.

A more comprehensive comparison can be achieved by considering the ignition delay times of *n*-dodecane measured by Vasu et al. [21], which was discussed above, in conjunction with the simulation results and the experimental data from Shen et al. [22]. In order to accomplish this, it is essential to consider pressure scaling laws appropriate at different temperature ranges. Note that both the groups, Vasu et al. and Shen et al., have scaled their ignition delay data to their respective nominal pressures using P^{-1} at all temperatures, and this can be assumed to be valid considering the small range of pressures which the individual experimental data sets span. However, the inverse pressure scaling would cease to be appropriate at temperatures in the NTC regime of ignition, which corresponds to temperatures, T 1000 K, in Fig. 10. A pressure scaling in the NTC region would involve a stronger relation, $\sim P^{-a}$, where $a > 1$ [55], due to the strong dependence of ignition delays in the NTC regime on the low temperature peroxy pathways. Gauthier et al. [56] have obtained a pressure scaling in the NTC ignition regime, that follows $\tau \propto P^{-1.64}$, by comparing the values of the peaks of the quadratic fits to the ignition delays of stoichiometric *n*-heptane/air mixtures at $P = 15–25$ atm. This is a simplified representation in which the dependence on temperature has been neglected as noted in Gauthier et al. In the absence of additional information to consider the variation in temperature, the above relationship is used to scale the ignition delays throughout the NTC regime of ignition.

Using the above scaling law, the ignition delay data from Vasu et al. [21] at pressures $P = 18–28$ atm has been scaled down to $P = 14$ and up to 40 atm, according to $P^{-1.64}$ for $T < 1000$ K, and P^{-1} for $T > 1000$ K, and included in Fig. 10. Considering these data sets together reveals some potential scatter between them, as well as discrepancies associated with the peak values of the ignition delay curve, at which ignition process transitions from the NTC regime of ignition to the high temperature ignition. The simulations agree closely with the scaled data of Vasu et al. in the NTC regime of ignition, $T \lesssim 1000\,K$, and this lends confidence to the ability of the present reaction mechanism to capture the pressure dependence in the NTC regime of ignition. Nevertheless, this aspect needs to be revisited when more information becomes available.

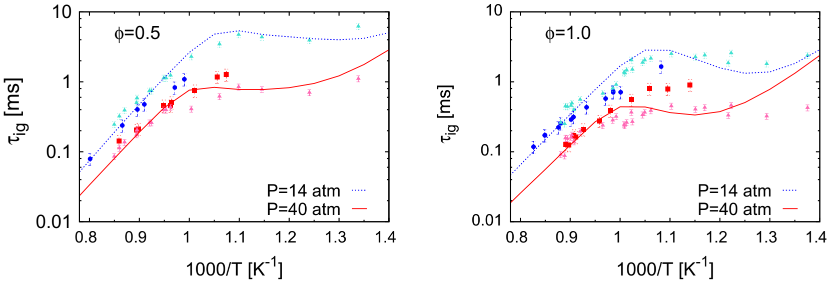

(a) $\phi = 0.5$ (b) $\phi = 1.0$

Fig. 10. Ignition delays of *n*-dodecane/air mixtures; lines – results obtained using the present reaction mechanism at $P = 14$ atm (····) and $P = 40$ atm (—); symbols – experiments: Shen et al. [22] at $P = 12–18$ atm and 38–46 atm, scaled to $P = 14$ atm (●) and $P = 40$ atm (■) respectively, using P^{-1} scaling law adopted in their study; Vasu et al. [21] data at $P = 18–28$ atm is scaled to $P = 14$ atm and $P = 40$ atm (cyan and pink triangles respectively) using P^{-1} scaling at $T > 1000$ K, and $P^{-1.64}$ scaling at $T < 1000$ K (see text). Ignition delays of *n*-dodecane are determined in the experiments of Shen et al. [22] by using the onset of OH emission (estimated uncertainty of ±20%), and the simulations follow the same ignition criteria.

3.1.3. Low temperature ignition: $T < 750$ K

Experimentally measured ignition delay time data for *n*-dodecane at low temperatures are scarce, and therefore, it would be appropriate to consider corresponding ignition data for other normal alkanes, which show similar ignition characteristics. Particularly, the low temperature ignition of *n*-heptane and *n*-decane have been the object of several shock tube [55,57] and rapid compression machine (RCM) studies [58,25]. Sarathy et al. [14] also measured ignition delays of *n*-octane/air mixtures at $T < 750$ K in a heated high-pressure shock tube.

When considering these experimental data sets together, some differences pertaining to the nature of the pressure scaling of ignition delays at low temperatures crop up. For instance, the ignition delays measured at low temperatures in the shock tube studies of Ciezki and Adomeit [55] for *n*-heptane, and Pfahl et al. [57] for *n*-decane (not shown here), exhibit no dependence on pressure. This is also supported by the analytical solutions for ignition delays in the low temperature ignition regime provided by Peters et al. [59] for *n*-heptane. On the contrary, Kumar et al. [25] report a $P^{-1.14}$ scaling to collapse their ignition delay data for *n*-decane measured in an RCM at low temperatures.

The experimental data from Kumar et al. [25] obtained at $\phi = 0.8$ and different pressures are shown in Fig. 11. The ignition delays of *n*-dodecane simulated at these experimental conditions are also shown in the same plot. The computations agree with the measurements at the lowest pressure examined, while predicting longer ignition delays compared to the data at higher pressures, which was also observed in the original Westbrook et al. [13] model. The predicted temperature dependence on ignition delays (i.e. the slope $d\tau/dT$) follows the experimental data at all pressures. However, they do not exhibit the strong dependence of ignition delays with variation in pressure shown by the experimental data. The negligible impact due to pressure change at these low temperatures depicted by the simulations, is in agreement with the observations made in the aforementioned studies [55,57,59].

Nonetheless, it appears that the variation of ignition delays with pressure cannot be entirely ruled out, and needs to be further investigated when a clear understanding emerges. It might be essential to incorporate a pressure dependent treatment of reactions important for ignition at these low temperatures, such as the unimolecular decomposition of the peroxy hydroperoxy dodecyl radical ($O_2C_{12}H_{24}OOH$) and ketohydroperoxide ($C_{12}KET$) radical, to reproduce the pressure scaling of ignition delays appropriately.

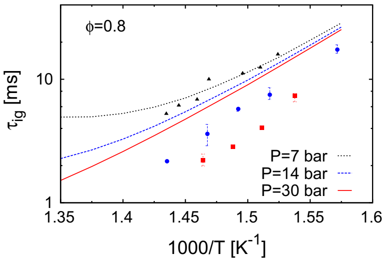

Fig. 11. Low temperature ignition delays of fuel/air mixtures at $\phi = 0.8$; symbols – experiments: Kumar et al. [25] for *n*-decane/air mixtures at pressures, $P = 7$ bar (▲), 14 bar (●), and 30 bar (■) (error bars as indicated); lines – ignition delays of *n*-dodecane/air mixtures computed using the present reaction mechanism, following the same color code as the experimental data points at different pressures. The measured ignition delays show a strong dependence on pressure variation, while this is not seen in the computations. However, the predicted trend is in agreement with the findings from other studies [55,57,59].

3.1.4. Remarks on ignition delay predictions

In order to summarize the ability of the present reaction mechanism to predict ignition delays, the experimental ignition delay data for several normal alkanes/air mixtures obtained at pressures ranging from 7–30 atm, are scaled to 20 atm according to the P^{-1} scaling at all temperatures, for both lean ($\phi = 0.5$) and stoichiometric alkane/air mixture conditions, and plotted in Fig. 12. These data sets at varied pressures are considered here merely for the sake of reference, and only qualitative comparisons are invoked, which allows the simplistic inverse pressure scaling law used above to be adequate for the following discussion. The ignition delays of *n*-dodecane/air mixtures computed using the present reaction mechanism (depicted by —) and the simulation results obtained using the detailed model of Sarathy et al. [14] (depicted by —) have also been included in Fig. 12.

As is evident from these plots, and as discussed in Section 3.1.2, the ignition delays obtained using the present reaction scheme closely follow the experimental data for *n*-dodecane at $T > 750$ K. As a consequence, they also fall well within the variability of the scaled experimental data at these temperatures. The computations display better predictions compared to the detailed model simulations at temperatures, $T > 750$ K, while at lower temperatures, these ignition delay predictions are identical to those of the detailed model, as seen from Fig. 12.

The slopes of the computed ignition delays at low temperatures are close to those suggested by the experiments at both equivalence ratios. Nevertheless, the agreement of these ignition delay predictions with the scaled RCM data from Kumar et al. [25] at $\phi = 0.5$ in Fig. 12(a) seems fortuitous in light of the observations made from Fig. 11, as well as the uncertainty prevailing in the pressure scaling at these low temperatures. Note that the simulations have been performed here using a constant UV model (shown by —), while a background pressure rise is often observed in experiments. A pressure gradient of $dP/dt = 1$–3%/ms was reported in the shock tube study of *n*-octane/air by Sarathy et al. [14], and a rise rate of $dP/dt = 1$–10%/ms was observed by Vasu et al. [21] during similar experiments for *n*-dodecane/air mixtures. It is therefore relevant to examine the effect of the background pressure rise rate in our simulated results.

Accordingly, the FlameMaster code [47] was modified by including a compression term in the temperature equation, as described in Pepiot [33]:

$$\frac{\partial T}{\partial t} = -\frac{\dot{\omega}_T}{\rho c_v} + \frac{1}{\rho c_p}\frac{dP}{dt}, \text{ where}$$

$$\dot{\omega}_T = \sum_{i=1}^{N_{\text{species}}} \left(h_i - \frac{RT}{W_i}\right)\dot{\omega}_i,$$

The notations h_i, $\dot{\omega}_i$, and W_i, denote the enthalpy, production rate, and molecular weight of species i, respectively. The ignition delays recomputed using a constant $dP/dt = 3\%$/ms in our calculations (shown by ……) are also included in Fig. 12. Including the pressure rise rate is found to result in <10% decrease in ignition delay times at temperatures, $T > 750$ K, for both equivalence ratios considered. In contrast, at lower temperatures, the influence of the pressure rise rate is much larger; the slope of the ignition delay time curve decreases, and the ignition time shortens for both fuel/air ratios. As a consequence, including the pressure rise rate in our calculations also results in better agreement between the simulations and the shock tube data of Sarathy et al. [14], especially at the lean equivalence ratio in Fig. 12(a).

3.2. Time histories of species profiles

In addition to the ignition delay time which is a global parameter, detailed measurements of the time histories of various species

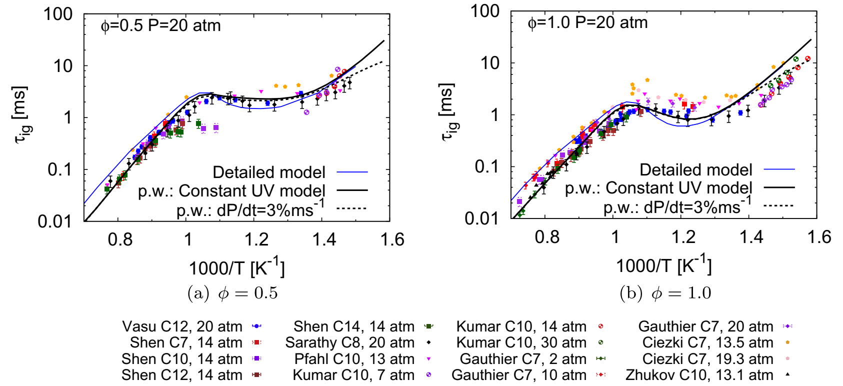

(a) $\phi = 0.5$ (b) $\phi = 1.0$

Fig. 12. Ignition delays of *n*-alkane/air mixtures from different experimental studies, scaled to a pressure of $P = 20$ atm using P^{-1} scaling law; symbols – experiments: Vasu et al. [21], Shen et al. [22], Sarathy et al. [14], Pfahl et al. [57], Kumar et al. [25], Ciezki and Adomeit [55], Gauthier et al. [56], Zhukov et al. [60]; solid lines denoted ignition delays of *n*-dodecane computed at $P = 20$ atm considering a constant UV model using (i) the present reaction mechanism (—), and (ii) the detailed mechanism of Sarathy et al. [14] (—); the differences in the simulation results obtained using the present kinetic scheme when considering a background pressure gradient of dP/dt = 3%/ms are shown by ⋯⋯.

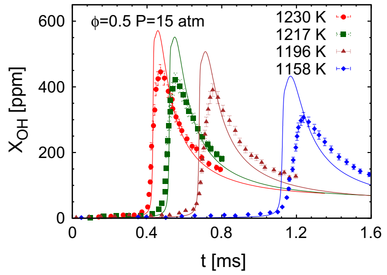

Fig. 13. OH concentration profiles during the oxidation of *n*-dodecane/O_2/argon mixtures in shock tubes as a function of time, at $P = 15$ atm and $\phi = 0.5$; symbols – experiments: Vasu et al. [21] (estimated uncertainly in X_{OH} of ±5%); lines – mole fractions of OH computed using the present reaction mechanism, following the same color code as the experimental data points at different temperatures. These results display an improved agreement with the measurements compared to those of the CPM model (the combined, prior to modifications model, whose results are shown in Fig. 4).

(OH, C_2H_4 etc.) serve as useful kinetic targets in assessing the individual rate parameters used in the reaction mechanism. First, the present model predictions are compared against the OH time histories measured in shock tubes by Vasu et al. [21] during the oxidation of *n*-dodecane/O_2/argon mixtures at $P = 15$ atm and $\phi = 0.5$. In Fig. 13, the computed OH profiles closely follow the measured rise of OH, displaying improved predictions compared to those of the CPM model, which is the combined model prior to the modifications introduced in Section 2.3 (see Fig. 4). Also the decay rate of OH is accurately predicted at all temperatures.

A reaction flux analysis was carried out to understand the consumption routes of OH at the experimental conditions of Vasu et al. [21] and $T = 1230$ K. As the reaction progresses to the ignition point, the OH radicals are initially consumed mainly by the H-abstraction by OH from the fuel, *n*-dodecane, to form the dodecyl radical and H_2O. The dodecyl radical further breaks up into smaller radicals and alkenes, and thereafter, the reactions of smaller alkenes + OH start contributing to the depletion of OH radicals. The decomposition of the radicals further produces C_2H_4 and C_3H_6, which then dominate the consumption of OH radicals among other alkenes. With the depletion of ethene and propene, the OH radical concentration builds up rapidly, eventually leading to ignition.

The importance of reactions involving smaller alkenes and their derivatives for predicting OH concentration is evident from the above discussion. The OH profiles at these experimental conditions are mostly influenced by the changes introduced in the present model to the rates of (i) alkene decomposition reactions, and (ii) alkenyl decomposition reactions, especially those forming A-C_3H_5 and C_5H_9 products, as described in Section 2.3. These rate changes result in an earlier rise in OH compared to the CPM model, and are crucial to capture the time instant of measured rise of OH concentration. The accompanied faster ignition also results in improved agreement with the ignition delay data corresponding to these experimental conditions, as evident from Fig. 7.

Davidson et al. [24] measured concentration profiles of different classes of species: reactant (*n*–$C_{12}H_{26}$), stable intermediate (C_2H_4), small radical pool representative (OH), reaction progress marker (H_2O) and products (CO_2) during the oxidation of stoichiometric *n*-dodecane/O_2/argon mixtures at $P = 2.25$ atm. In Fig. 14, the species profiles computed at these conditions agree well with the experiments for a major part of the studied time interval.

The fuel decay approximately follows the experimental data at the temperatures investigated in Fig. 14(a), although differences can be seen with the time scales of complete fuel depletion. The agreement of the predicted yields of the intermediate species C_2H_4 with the experimental data in Fig. 14(b) suggests that the branching ratios of the major decomposition pathways of *n*-dodecane to smaller alkyl radicals, which eventually lead to C_2H_4 in the products, are appropriate. The discrepancies between the simulated results and the experiments for C_2H_4 concentrations at early times are consistent with the fuel decay profiles shown in Fig. 14(a), where a faster fuel depletion rate at $T = 1390$ K leading to better agreement with the experiments, would result in a corresponding early rise in C_2H_4 concentration. The predicted time scales for C_2H_4 consumption are longer compared to the experiments.

In Fig. 14(c), the plateaus shown in the experimental OH profiles are observed in the simulations as well. The predicted post ignition levels of CO_2 and H_2 O in Fig. 14(d) and (e) respectively, are in agreement with the experimental data. The rise of CO_2 occurs largely as suggested by the experiments, and the predicted H_2O profile closely follows the experiments, an indication that the reaction progress is described accurately by the present reaction scheme.

Ignition delay measurements and sensitivity analysis

Davidson et al. [24] also reported ignition delay times at the same conditions as those discussed above, based on the time to reach 50% peak OH concentration. The simulation results are compared against these experimental data in Fig. 15. The computed ignition delays are longer compared to the measurements at $T < 1500$ K, while closely agreeing with the experimental data at

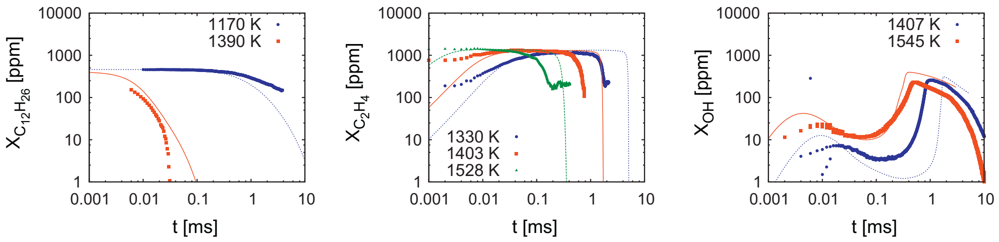

(a) $n\text{–}C_{12}H_{26}$ (b) C_2H_4 (c) OH

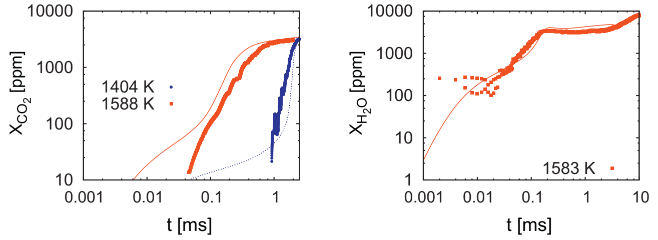

(d) CO_2 (e) H_2O

Fig. 14. Species mole fractions during the oxidation of n-dodecane/O_2/argon mixtures in shock tubes as a function of time, at $\phi = 1.0$ and $P = 2.25$ atm; symbols – experiments: Davidson et al. [24] (estimated uncertainly in X_{OH} of 3%); lines – species concentrations computed using the present reaction mechanism, following the same color code as the experimental data points for different species at different temperatures.

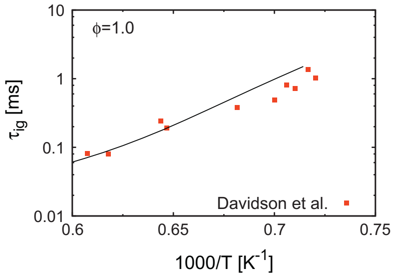

Fig. 15. Ignition delays of n-dodecane/O_2/argon mixtures at $\phi = 1.0$, $P = 2.2$ atm, and low initial fuel concentration, $X^0_{\text{fuel}} = 400$ ppm; symbols – experiments: Davidson et al. [24]; lines – ignition delays computed using the present reaction mechanism. Ignition delay times in the experiments [24] as the time to half-peak concentration for OH, and the simulations follow the same ignition criteria.

higher temperatures. This can also be inferred from the OH profile comparisons, where the rise of OH concentration at 1545 K follows the experimental measurements closely, while the computed rise of OH at 1407 K occurs later than the experiments in Fig. 14(c). At these higher temperatures, $T > 1400$ K, the OH profiles are little impacted by the rate changes involving alkene and alkenyl decomposition reactions described in Section 2.3, owing to the faster rates of these reactions at the higher temperatures.

In order to understand the differences in the time scales between the simulations and the experiments, a sensitivity analysis study was carried out to identify the reactions important to predict the ignition delays at $T \sim 1400$ K. The results of this analysis are summarized in Fig. 16. The importance of reactions involving propene, allyl, and allene is evident from this diagram. The reactions among smaller radicals and HO_2, such as reactions (7) and (8) discussed in Section 2.3, are not significant at these experimental conditions, which are at lower pressures and higher temperatures compared to those of Vasu et al. [21], due to the dominance of the branching reaction, $H + O_2 \rightarrow OH + O$, over the recombination reaction, $H + O_2 + M \rightarrow HO_2 + M$.

Considering the reactions among alkenes in Fig. 16, the ignition delays at these experimental conditions are sensitive to the rate of reversible reaction of allyl forming allene and H atom, as

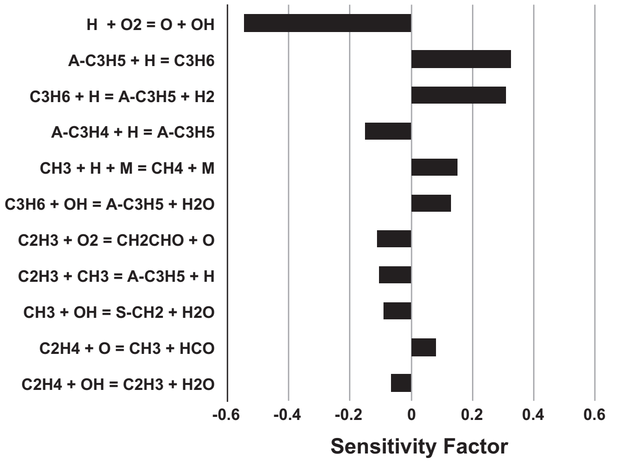

Fig. 16. Sensitivity analysis for ignition delays of n-dodecane/O_2/argon mixtures at $\phi = 1.0$, $P = 2.2$ atm, initial fuel mole fraction $X^0_{\text{fuel}} = 400$ ppm, and $T = 1403$ K. Sensitivities are determined by multiplying each rate constant by a factor of 2, and finding the change in ignition delays due to the rate change. Only those reactions with sensitivities >6% are reported here.

$$\text{A-}C_3H_5 \leftrightarrow \text{A-}C_3H_4 + H. \tag{11}$$

Allene further forms acetylene and methyl radicals upon H atom addition, given by

$$\text{A-}C_3H_4 + H \leftrightarrow C_2H_2 + CH_3. \tag{12}$$

In addition to reaction (11), the detailed reaction mechanism of Sarathy et al. [14] also includes a reaction whose reverse forms methyl and acetylene from allyl radicals directly, as

$$\text{A-}C_3H_5 \rightarrow C_2H_2 + CH_3. \tag{13}$$

The reaction rate used in the detailed model is similar to that recommended by the theoretical study of Diau et al. [61]. The elementary reactions (11)–(13) were considered in a later RRKM calculation by Davis et al. [62], and these authors prescribed a rate for reaction (13) that is five orders smaller than the Diau et al. recommendation at $T > 1300$ K. The discrepancy was due to the fact that the allyl dissociation to A-C_3H_4 and H atom, given by reaction (11), had not been accounted for in the Diau et al. calculations, while including this was found to have a significant influence on the rate coefficients of reaction (13) determined in the Davis et al. study. We found that incorporating the higher rate for reaction (13) used in the Sarathy et al. [14] model instead of the Davis et al. rate makes ignition time shorter, thus reproducing adequately the experimental C_2H_4 fall off time scales. This is because the pathway (13) above competes with the major consumption channel of A-C_3H_5, the addition of H atom to form C_3H_6, as

$$\text{A-}C_3H_5 + H \rightarrow C_3H_6. \qquad (14)$$

Therefore, with the enhanced rate for reaction (13), the amount of A-C_3H_5 consumption that proceeds via reaction (14) is reduced, and it can be readily observed from the sensitivity analysis shown in Fig. 16, that an effective decrease in the rate of this reaction would decrease the time to ignite.

Nevertheless, following the more complete calculations of Davis et al. [62], since some uncertainty remains in the rate calculated by Diau et al. [61] for reaction (13), the present reaction mechanism does not incorporate reaction pathway (13), and the species profile and ignition delay time predictions remain unchanged from Figs. 14 and 15, respectively. The authors believe that improvement to the time scales associated with the species profile predictions requires more accurate rate determinations of the reactions among the C_3 species identified here as important from sensitivity analysis.

3.3. Oxidation and pyrolysis in shock tubes

Mole fractions of the stable species produced during the oxidation and pyrolysis of *n*-dodecane were measured by Malewicki and Brezinsky [43] in a heated high pressure single pulse shock tube, at fixed reaction times, as a function of reactor temperature. Their experimental data was obtained for *n*-dodecane/O_2/argon mixtures at moderate to high temperatures, $T = 867–1739$ K, varied pressures, $P = 19–74$ atm, and equivalence ratios, $\phi = 0.46$, 1.06, 2.05, and ∞. The reaction time at which the mole fractions were reported is defined as the time duration between the initial pressure rise due to the incident shock reflection and the time to reach 80% of the maximum pressure rise, and varied between 1.15–3.47 ms at different temperatures.

The experimental set up is modeled here using constant volume simulations at the exact fuel/O_2/argon compositions, pressures, temperatures, and reaction times, reported in the data sets. No ignition is observed in the present simulations as well as the experiments even though the reaction times reported are longer than the typical ignition delays at these temperatures since the mixtures that were investigated are dilute with $X_{\text{fuel}} < 100$ ppm.

The results of the computations are shown in Fig. 17 for lean *n*-dodecane oxidation at pressures 41.0–61.2 atm (nominal pressure, $P_{\text{NOM}} = 50$ atm) along with the experimental data. The simulations at stoichiometric and rich conditions also showed similar comparisons with the corresponding measurements. The simulations follow the fuel decay accurately in Fig. 17(a). At $T \sim 900$ K, little reactivity is observed, and as the initial temperature is increased above $T \sim 1040$ K in Fig. 17(a), the fuel decay occurs rapidly. The fuel is completely consumed, and CO and CO_2 begin to form in Fig. 17(b) at temperatures $T \sim 1100$ K. The changes introduced to the rates of H-abstraction from the fuel by HO_2, and the decomposition reactions of alkenes and alkenyl radicals, described in Section 2.3, advance the temperature at which fuel decay begins by about 40 K, thereby improving the agreement between the simulated fuel decay profile and the experimental data. Similarly improved predictions in the rise of CO, ethane, and smaller alkenes profiles, in Fig. 17(b)–(d), also result from these modifications to the present model. The predicted oxidizer concentrations in Fig. 17(a) agree with the experiments at temperatures below 1200 K and above 1400 K, while showing slower consumption rates than the experimental data at the temperatures in between.

A reaction flux analysis was performed to investigate the fuel decay pathways at different temperatures. At the highest temperatures, $T \sim 1600$ K, the fuel is consumed at short time scales by oxygen-free pathways. These involve (i) unimolecular fuel decomposition pathways that produce smaller radicals, which in turn, generate H atoms, and (ii) subsequent H-abstractions by H atoms from the fuel, resulting in a rapid decay of the fuel. At temperatures, $T < 1400$ K, in addition to the H-abstractions by H atoms, the H-abstractions by OH radicals also contribute to a significant portion of the fuel decay, and dominate over the H-abstractions by H atoms as a major fuel decay route at lower temperatures, $T \sim 1050$ K. However, due to the dilute fuel/oxidizer mixture, there is little oxidizer (<4%) that is used up to generate the OH radicals required to consume the fuel. This is particularly evident at $T < 1100$ K in Fig. 17(a), where there is almost negligible consumption of the oxidizer accompanied with the fuel decay. The significant consumption of the oxidizer seen at $T > 1100$ K, occurs only at later times, after the fuel has been consumed entirely.

In Fig. 17(d), the concentrations of ethylene and propene build up simultaneously as the fuel decays at $T \sim 1040$ K, via the unimolecular decomposition pathways of the fuel and the break up of the resulting smaller radical products. This is also accompanied by the production of smaller alkanes, ethane and methane, as the radical pool continues to build up, as seen from Fig. 17(c). The decay of C_2H_4 contributes to the formation of acetylene in Fig. 17(d) at $T \sim 1200$ K. The predicted alkene and alkane concentrations fall within the uncertainty in the experimental data at temperatures where their concentrations increase. A shift is seen in their predicted decay profiles compared to the experimental data at higher temperatures in Fig. 17(c) and (d). A similar shift is also seen in Fig. 17(b), with regard to the predicted CO and CO_2 profiles compared to the experiments at higher temperatures.

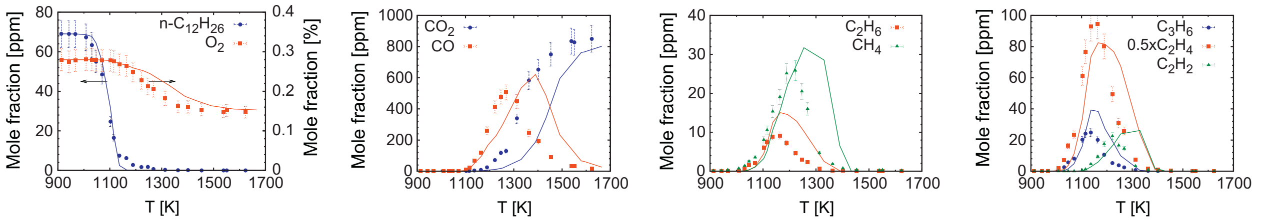

(a) Fuel and oxidizer (b) Carbon oxides (c) Small alkanes (d) Small alkenes and acetylene

Fig. 17. Mole fractions of major species during the oxidation of lean *n*-dodecane/O_2/argon mixtures at $\phi = 0.46$ and a nominal pressure of $P_{\text{NOM}} = 50$ atm; symbols – experiments from Malewicki and Brezinsky [43] (estimated uncertainty of ±10%); lines – results computed using the present reaction scheme, following the same color code as the experimental data points for different species profiles.

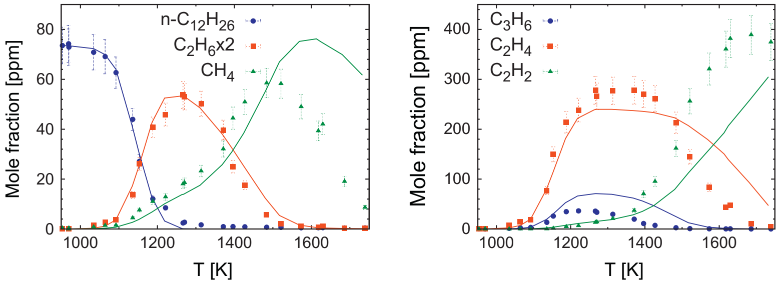

(a) Fuel and small alkanes (b) Small alkenes and acetylene

Fig. 18. Mole fractions of major species during the pyrolysis of *n*-dodecane at a nominal pressure of $P_{NOM} = 22$ atm; symbols – experiments from Malewicki and Brezinsky [43] (estimated uncertainty of ±10%); lines – results computed using the present reaction mechanism, following the same color code as the experimental data points for different species profiles.

Malewicki and Brezinsky [43] also measured species concentrations at pyrolytic conditions and nominal pressures of $P = 22$ and 50 atm. A comparison between the predicted species concentrations and the measurements at pressures ranging from $P = 19.5$–26.6 atm is shown in Fig. 18. The decay of the fuel is well captured by the simulation results in Fig. 18(a). The pathways that govern the fuel consumption are the same as the oxygen-free decomposition routes discussed earlier in connection with the oxidation case. The contributions of the unimolecular fuel decomposition pathways dominate over the H-abstraction reactions by H atoms as the major fuel decay route at the higher temperatures ($T \sim 1600$ K), while the reverse is true at the lower temperatures ($T \sim 1050$ K).

The computed ethane concentrations in Fig. 18(a) show excellent agreement with the experimental data. While the predicted concentrations of methane falls within the experimental uncertainties at $T < 1500$ K, the concentrations are over-predicted at higher temperatures. Similar trends are also seen with the ethene and acetylene profiles in Fig. 18(b). The propene concentrations are over-predicted compared to the experimental data. Nevertheless, the comparison of the simulated results obtained using the present reaction mechanism with the experimental measurements for the pyrolysis and oxidation cases remains favorable.

3.4. Pressurized flow reactor studies

Kurman et al. [26] studied the oxidation of *n*-dodecane in a pressurized flow reactor over the low and moderate temperature regime (550–830 K), at a pressure of $P = 8$ atm, and lean equivalence ratio, $\phi = 0.23$. Figure 19 shows the concentrations of fuel, oxidizer, major intermediates, and products as a function of sample temperature at a residence time $\tau_{res} = 120$ ms. The NTC behavior can be seen in Fig. 19(a) with high fuel reactivity at $T \sim 700$ K, and lower reactivity at higher temperatures. At the sample temperature of maximum reactivity, $T \sim 670$ K, the fuel is primarily consumed via H-abstraction by OH radicals. The oxidizer profile in Fig. 19(b) follows the fuel consumption, showing large oxygen consumption when the fuel reactivity is high, and the computed oxygen mole fraction shows satisfactory agreement with the experimental data for the entire temperature range.

In Fig. 19(c), the computed H_2 O profile varies in accordance to that suggested by the experiments, however, the concentration is under-predicted by ~30% when compared to the experimental data. This trend is consistent with the over-prediction in CO concentration and under-prediction in CO_2 concentration, observed in the simulations in Fig. 19(d) and (e) respectively, tied together by an insufficient amount of OH in the reaction pool at these experimental conditions.

In their chemical kinetic scheme for the oxidation of *n*-heptane/iso-octane mixtures, Glaude et al. [63] note the importance of secondary reactions of cyclic ethers, which involve pathways that could contribute to CO_2 at these low temperatures, in addition to the $CO + OH \rightarrow CO_2 + H$ reaction, as well as produce OH radicals by a branching reaction. Their branching pathway is the familiar low temperature oxidation pathway of alkanes, now applied to a cyclic ether. In short, the lumped radical obtained by H-abstraction from the cyclic ether by OH, adds an oxygen molecule, followed by isomerization, second oxygen addition, second isomerization, and a β-scission to form the analoges of ketohydroperoxides. This is followed by a branching reaction that gives OH radical and several C_0–C_2 species, including CO_2. This pathway was found to contribute significantly to the CO_2 predicted by their reaction mechanism at $T \sim 650$ K in Jet-Stirred Reactor (JSR) simulations.

In the Sarathy et al. [14] model, and therefore in the present model, the cyclic ethers formed from hydroperoxy dodecyl radicals upon addition with OH are assumed to decompose into a carbonyl radical RCO, H_2O, and a corresponding smaller alkene. In the present work, the importance of the secondary reaction pathways for cyclic ether oxidation suggested by Glaude et al. [63] was examined, by adding a set of reactions among relevant lumped species to the present reaction mechanism. The rate constants for these reactions were assigned analogous to the corresponding reactions in the low temperature chemistry of alkanes. Nonetheless, these additional pathways did not result in any difference to the species profiles at the conditions investigated here. The simulated results turned out to be identical to those shown in Fig. 19(a)–(e), and therefore, these secondary pathways are not retained in the present reaction mechanism. The differences prevailing between the experimental data and the simulations need to be understood better.

Veloo et al. [27] also measured CO profiles in the Princeton variable pressure flow reactor during the oxidation of *n*-dodecane/O_2/N_2 mixtures at stoichiometric conditions, $P = 8$ atm, and temperatures ranging from 500–1000 K. The temperature range studied allowed for the demarcation of the two stage auto-ignition characteristics of *n*-dodecane. The concentration profiles were reported as a function of the initial reactor temperature, at a fixed residence time, $\tau_{res} = 1$ s. Only a qualitative comparison of the simulations with the experimental data would be appropriate here to allow for time shift corrections, as advised by Veloo et al. [27].

A comparison of the computed CO profile against the experimental data is shown in Fig. 19(f). An over-prediction in CO is observed at all temperatures considered here. At lower temperatures ($T < 750$ K), this is consistent with the observations made previously when comparing with the Kurman et al. [26] data. At higher

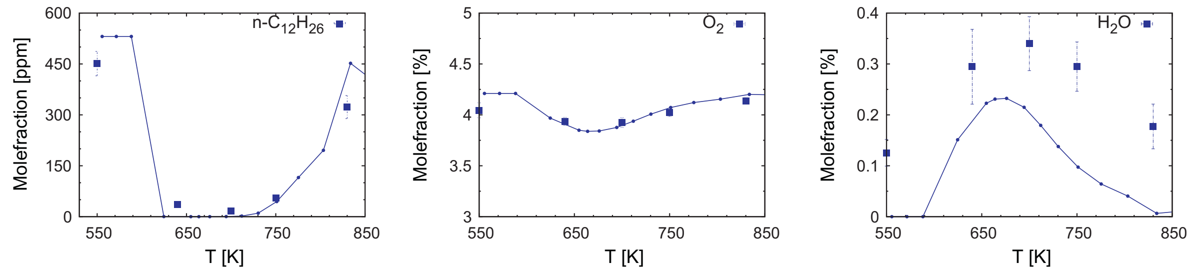

(a) n-$C_{12}H_{26}$ (b) O_2 (c) H_2O

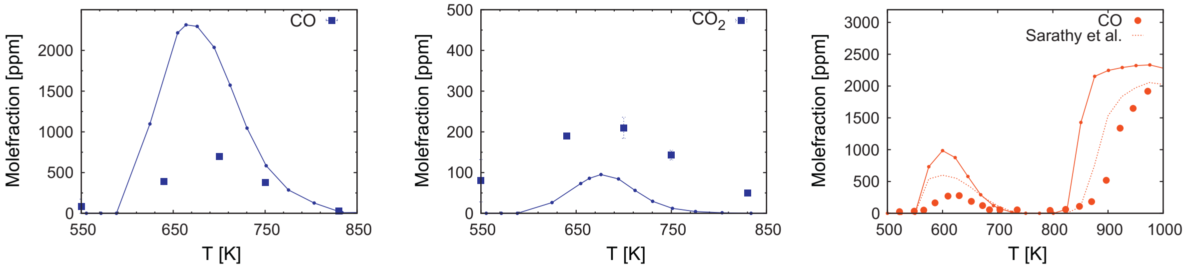

(d) CO (e) CO_2 (f) CO

Fig. 19. Concentrations of major species measured in pressurized flow reactors at $P = 8$ atm, as a function of sample temperature, at a fixed residence time (τ_{res}): (a)–(e): Lean ($\phi = 0.23$) oxidation of n-dodecane/air at $T = 550$–830 K, $\tau_{res} = 120$ ms; symbols – experiments: Kurman et al. [26] (■) (error bars as indicated), (f) Stoichiometric ($\phi = 1.0$) oxidation of n-dodecane/air at $T = 550$–1000 K, $\tau_{res} = 1$ s; symbols – experiments: Veloo et al. [27] (●) (estimated uncertainty in $X_{CO} < 3\%$), reproduced with permission from the authors; lines – mole fractions computed using the (i) present reaction mechanism (—, —), and (ii) detailed scheme of Sarathy et al. [14] (·····), shown for the sake of comparison.

temperatures, the experimental data suggest a transition out of the NTC regime at a temperature of 850 K, whereas the model predicts an early transition at 825 K.

Also plotted in Fig. 19(f) are the CO concentrations computed using the detailed mechanism of Sarathy et al. [14], which show better agreement in terms of transition temperature compared to the present kinetic scheme. This discrepancy can be linked to the difference in base chemistry, especially regarding the $CH_2CHO + O_2$ pathways. In addition, the temperature at which the CO profile rises is also influenced by some of the changes made in the present reaction mechanism, namely the modifications to the H-abstraction rate from the fuel by HO_2, and the alkenyl decomposition reaction rates, discussed in Section 2.3. However, these revisions have been introduced conforming to existing sources in literature, and they lead to improved results for validation cases at higher temperatures, $T > \sim 1000$ K, such as ignition delays, OH profiles, and major species profiles, discussed previously in the current section. Their influence on the present test case at $T < 850$ K suggests a possible temperature dependence for these reaction rates, which would give a better agreement for both the high as well as low temperature validation cases.

3.5. Burning velocities

3.5.1. n-dodecane/air mixtures

Kumar and Sung [45] measured laminar flame speeds of n-dodecane/air mixtures for a range of equivalence ratios using a counterflow twin-flame technique, at atmospheric pressure, and pre-heat temperatures of $T_u = 400$ K and 470 K. Ji et al. [28] also measured flame speeds at $P = 1$ atm and $T_u = 403$ K. Recently, another set of flame speed data for n-dodecane/air mixtures, at pressures of 1–3 atm and $T_u = 400$ K has been made available by Hui and Sung [46].

Figure 20 shows the computed flame speeds of n-dodecane in comparison to the experimental data. The effect of varying pre-heat temperatures and pressures are shown in Fig. 20(a) and (b), respectively. The computations show excellent agreement with the more recent non-linearly extrapolated data from Hui and Sung [46] at $T_u = 400$ K and varying pressures. At the higher pre-heat temperature of $T_u = 470$ K, in Fig. 20(a), the simulations agree with the experimental measurements of Kumar and Sung [45] on the fuel lean side, while showing some differences on the rich side.

However, upon comparing the experimental data from Kumar and Sung at $T_u = 403$ K with the n-dodecane flame speeds measured by Ji et al. [28] and Hui and Sung [46] at this unburnt temperature, it seems that the Kumar and Sung data are on the higher end for rich fuel/air mixtures, especially at $\phi > 1.2$. Supposing this trend to persist at higher pre-heat temperatures, the under-prediction observed in the simulated flame speeds at $T_u = 470$ K compared to Kumar and Sung data for fuel rich conditions, appears to be appropriate. Additional data at these higher pre-heat temperatures are required to make conclusive remarks about the capabilities of the model to predict laminar flame speeds at these conditions.

3.5.2. n-alkane/air mixtures

Davis and Law [64,65] measured laminar flame speeds for small alkanes and found the burning speeds at a given equivalence ratio to be nearly identical for n-alkanes from C_4–C_7 at atmospheric pressure. Ji et al. [28] extended this trend of similarity all the way to n-dodecane at atmospheric pressure. Kelley et al. [29] measured laminar flame speeds for C_5–C_8 n-alkanes, at higher pressures, and confirmed the fuel similarity to be manifest at elevated pressures as well. To evaluate the ability of the present model to predict laminar flame speeds at elevated pressures, and lower pre-heat temperatures, we seek to exploit the fuel similarity exhibited by n-alkanes.

The laminar flame speeds of n-alkanes/air mixtures measured by Kelley et al. [29] and Ji et al. [28] at $T_u = 353$ K and $P = 1$ atm,

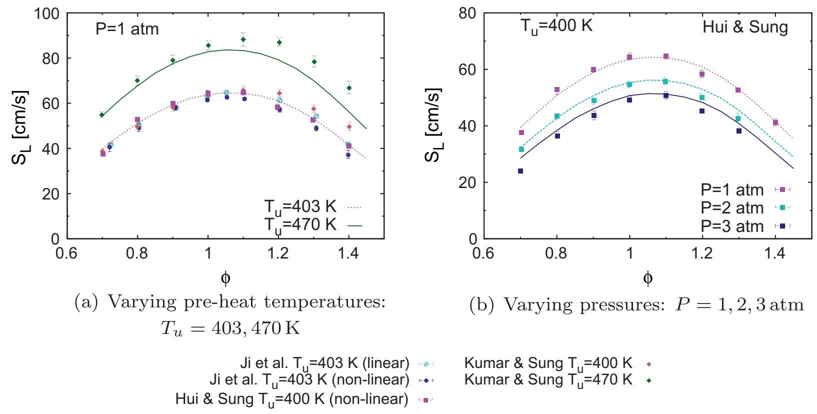

(a) Varying pre-heat temperatures: $T_u = 403, 470\,\mathrm{K}$

(b) Varying pressures: $P = 1, 2, 3\,\mathrm{atm}$

Fig. 20. Laminar flame speeds of *n*-dodecane/air mixtures as a function of equivalence ratio at (a) varying pre-heat temperatures, $T_u = 403, 470$ K at $P = 1$ atm, and (b) varying pressures $P = 1, 2, 3$ atm at $T_u = 400$ K; symbols – experiments: Kumar and Sung [45], Ji et al. [28], Hui and Sung [46] (error bars as indicated); lines – *n*-dodecane/air flame speeds computed using the present reaction mechanism.

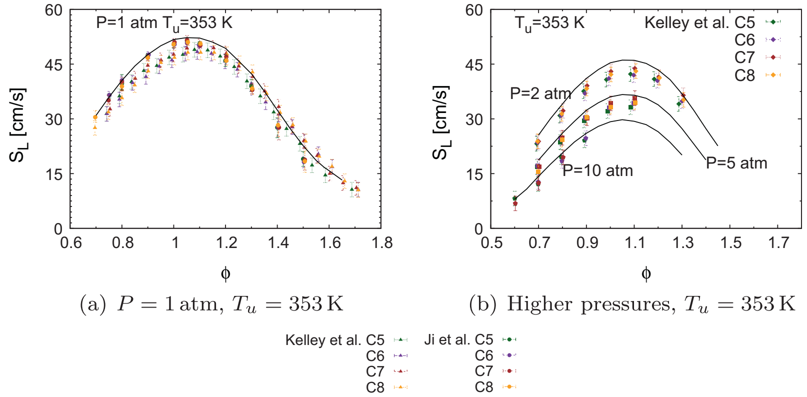

(a) $P = 1\,\mathrm{atm}$, $T_u = 353\,\mathrm{K}$

(b) Higher pressures, $T_u = 353\,\mathrm{K}$

Fig. 21. Laminar flame speeds of *n*-dodecane/air mixtures compared with flame speed measurements of smaller *n*-alkane/air mixtures; symbols – experiments: Ji et al. [28] (error bars as indicated), Kelley et al. [29] (uncertainty of ±2 cm/s); lines – *n*-dodecane/air flame speeds computed using the present reaction scheme. Similarity in *n*-alkane/air flame speeds is invoked here to assess the ability of the present reaction mechanism to predict flame speeds at higher pressures and lower pre-heat temperatures than those considered in Fig. 20.

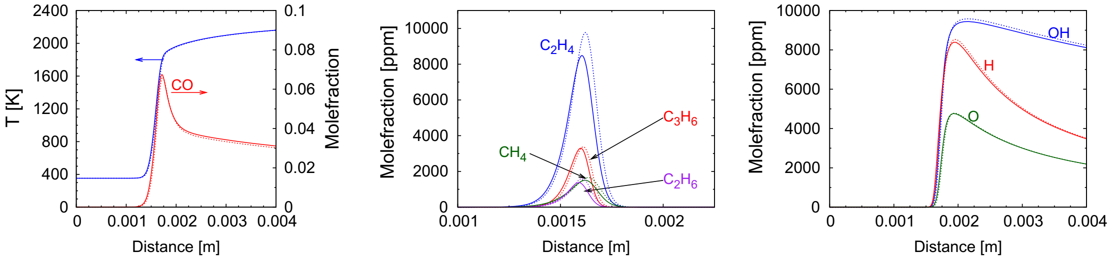

(a)

(b)

(c)

Fig. 22. Analyzing the structures of *n*-dodecane (——) and *n*-heptane (·····) premixed flames at stoichiometric conditions using the present reaction mechanism at $P = 1$ atm and $T_u = 353$ K. The similar variation of temperature, CO, and small radical concentrations (H, O, OH) between *n*-heptane and *n*-dodecane support fuel similarity and consistency within the reaction mechanism.

and the flame speeds of *n*-dodecane/air mixtures computed at these experimental conditions are shown in Fig. 21(a). At all fuel/air ratios, the computed flame speeds lie within the band of flame speeds suggested by the combined experimental data from Kelley et al. and Ji et al. For lean mixtures, the computed flame speeds agree closely with the Ji et al. data, while for rich mixtures, the predicted flame speeds reproduce the Kelley et al. data better. The over-prediction of computed flame speeds at $T_u = 353$ K compared to the non-linearly extrapolated flame speed data from Ji et al. at rich mixture conditions was also observed at $T_u = 403$ K, as seen from Fig. 20(a).

Comparing the computed flame speeds against the measurements made by Kelley et al. [29] at higher pressures of $P = 2$, 5, and 10 atm, shown in Fig. 21(b), it can be seen that the computed flame speeds are within the uncertainties in the experimental data at all pressures. In addition, the agreement between the computations and the experimental data improve with increasing pressure, a welcome trend, since the reaction mechanism developed in the present work is likely to be applied in engine-like elevated pressure environments.

Following the analysis by Kelley et al. [29], the similarity exhibited by the normal alkanes can be further explored by considering flame speeds and species concentrations in premixed flames of *n*-heptane, which is part of the base model. At $P = 1$ atm, $T_u = 353$ K, and $\phi = 1.0$, the computed flame speeds of *n*-dodecane/air and *n*-heptane/air mixtures are very close, 51.5 cm/s and 52.9 cm/s, respectively. Figure 22(a) shows very similar temperature profiles for the two fuels as a function of distance along the flame. This is also true of the CO profiles, indicative of similar heat release for the two fuels, consistent with similar flame speeds. In Fig. 22(b), the concentrations of C_2 and C_3 species whose profiles depend on the unimolecular fuel decomposition routes from *n*-heptane and *n*-dodecane show differences. However, the profiles for the key radicals, H, O, and OH, shown in Fig. 22(c) for the two fuels are virtually identical, further supporting fuel similarity and consistency within the reaction mechanism.

4. Conclusions

With the long term objective of a kinetic model for jet fuel surrogates, a reaction mechanism has been developed to describe the oxidation of a representative paraffin molecule, *n*-dodecane. This has been accomplished by starting with a chemical mechanism proposed earlier for smaller hydrocarbons along with a few substituted aromatics [1,4] as base model, and extending this model to include the reaction pathways of *n*-dodecane oxidation. Starting with the LLNL detailed mechanism for methyl alkanes and *n*-alkanes proposed by Sarathy et al. [14], a skeletal level mechanism for *n*-dodecane oxidation was obtained using reaction mechanism reduction techniques, which was then incorporated into the previous scheme. Rate changes were introduced to this combined model motivated by sensitivity studies and supported by recommendations from literature. The resulting revised mechanism was comprehensively validated for *n*-dodecane oxidation against various experimental data sets.

The validation test cases included ignition delays, species time histories, and major species concentration profiles measured in shock tubes, laminar burning velocity measurements, and major species profiles in a pressurized flow reactor configuration. Similarity in ignition delays and laminar flame speeds among normal alkanes was invoked to assess the kinetic model, thereby complementing the existing experimental data. The ability of the present reaction mechanism in predicting different targets has been discussed in detail. It is worth re-emphasizing that the present work has undertaken for the first time an extensive validation by comparing against a wide range of experimental data that have become available in the last couple of years. The ability of the present model to adequately describe the ignition behavior for low through high temperatures is also noteworthy. The key contribution of this work is that the proposed reaction mechanism can describe the kinetics of *n*-dodecane, as well as that of *n*-heptane, iso-octane, and substituted aromatics considered in our previous works [1,4], which are important components of transportation fuel surrogates.

The model described here, as well as a derived model relevant to high temperature oxidation only, along with the corresponding thermodynamic and transport properties have been made available as Supporting Materials. The performance of this high temperature model has been verified to be similar to the complete model at $T > 1100$ K. The validation cases used in this work were repeated for this high temperature model, and are made available with the Supporting materials (Figs. S27–S33) for the sake of completeness.

Acknowledgments

The first and the third author gratefully acknowledge funding by the Air Force Office of Scientific Research and NASA. The second author acknowledges support from the Department of Energy under Grant DE-FG02-90ER14128. The third author also acknowledges support from the German Research Foundation (DFG) within the Collaborative Research Centre SFB 686 – Model-Based Control of Homogenized Low-Temperature Combustion at RWTH Aachen University, Germany, and Bielefeld University, Germany. The first author would like to thank Liming Cai for the discussions on H_2/O_2 chemistry and Sivaram Ambikasaran for his valuable comments on the manuscript. The authors would like to thank Dr. Veloo, Dr. Jahangirian, and Dr. Dryer for permitting to use their experimental data.

Appendix A. Supplementary material

Supplementary data associated with this article can be found, in the online version, at http://dx.doi.org/10.1016/j.combustflame.201 3.10.012.

References

[1] G. Blanquart, P. Pepiot-Desjardins, H. Pitsch, Chemical mechanism for high temperature combustion of engine relevant fuels with emphasis on soot precursors, Combust. Flame 156 (2009) 588–607.
[2] T. Edwards, Kerosene fuels for aerospace propulsion-composition and properties, in: 38th AIAA/ASME/SAE/ASEE Joint Propulsion Conference & Exhibit, 2002, pp. 2002–3872.
[3] L.M. Shafer, R.C. Striebich, J. Gomach, T. Edwards, Chemical class composition of commercial jet fuels and other specialty kerosene fuels, in: 14th AIAA/AHI Space Planes and Hypersonic Systems and Technologies Conference, 2006, pp. 2006–7972.
[4] K. Narayanaswamy, G. Blanquart, H. Pitsch, A consistent chemical mechanism for the oxidation of substituted aromatic species, Combust. Flame 157 (10) (2010) 1879–1898.
[5] A. Violi, S. Yan, E. Eddings, A. Sarofim, S. Granata, T. Faravelli, E. Ranzi, Experimental formulation and kinetic model for JP-8 surrogate mixtures, Combust. Sci. Technol. 174 (11–12) (2002) 399–417.
[6] K. Narayanaswamy, P. Pepiot, H. Pitsch, Jet fuels and Fischer-tropsch fuels: surrogate definition and chemical kinetic modeling, in: U.S National Combustion Meeting, 2013.
[7] M. Colket, T. Edwards, S. Williams, N.P. Cernansky, D.L. Miller, F. Egolfopoulos, P. Lindstedt, K. Seshadri, F.L. Dryer, C.K. Law, D. Friend, D.B. Lenhert, H. Pitsch, A. Sarofim, M. Smooke, W. Tsang, Development of an experimental database and kinetic models for surrogate jet fuels, in: 45th AIAA Aerospace Sciences Meeting and Exhibit, 2007, pp. 2007–2770.
[8] K.D. Dahm, P.S. Virk, R. Bounaceur, F. Battin-Leclerc, P.M. Marquaire, R. Fournet, E. Daniau, M. Bouchez, Experimental and modelling investigation of the thermal decomposition of n-dodecane, J. Anal. Appl. Pyrol. 71 (2004) 865–881.
[9] O. Herbinet, P. Marquaire, F. Battin-Leclerc, R. Fournet, Thermal decomposition of *n*-dodecane: experiments and kinetic modeling, J. Anal. Appl. Pyrol. 78 (2007) 419–429.
[10] J. Biet, M.H. Hakka, V. Warth, P. Glaude, F. Battin-Leclerc, Experimental and modeling study of the low-temperature oxidation of large alkanes, Energy Fuels 22 (4) (2008) 2258–2269.
[11] E. Ranzi, A. Frassoldati, S. Granata, T. Faravelli, Wide-range kinetic modeling study of the pyrolysis, partial oxidation and combustion of heavy *n*-alkanes, Int. Eng. Chem. Res. 44 (2005) 5170–5183.
[12] A. Mzé-Ahmed, K. Hadj-Ali, P. Dagaut, G. Dayma, Experimental and modeling study of the oxidation kinetics of *n*-undecane and *n*-dodecane in a jet-stirred reactor, Energy Fuels 26 (7) (2012) 4253–4268.
[13] C.K. Westbrook, W.J. Pitz, O. Herbinet, H.J. Curran, E.J. Silke, A detailed chemical kinetic reaction mechanism for *n*-alkane hydrocarbons from *n*-octane to *n*-hexadecane, Combust. Flame 156 (1) (2009) 181–199.
[14] S.M. Sarathy, C.K. Westbrook, M. Mehl, W.J. Pitz, C. Togbe, P. Dagaut, H. Wang, M.A. Oehlschlaeger, U. Niemann, K. Seshadri, Comprehensive chemical kinetic modeling of the oxidation of 2-methylalkanes from C_7 to C_{20}, Combust. Flame 158 (12) (2011) 2338–2357.
[15] D. Healy, N.S. Donato, C.J. Aul, E.L. Petersen, C.M. Zinner, G. Bourque, H.J. Curran, *n*-butane: ignition delay measurements at high pressure and detailed chemical kinetic simulations, Combust. Flame 157 (8) (2010) 1526–1539.
[16] H.J. Curran, P. Gaffuri, W.J. Pitz, C.K. Westbrook, A comprehensive modeling study of *n*-heptane oxidation, Combust. Flame 114 (1–2) (1998) 149–177.

[17] H.J. Curran, P. Gaffuri, W.J. Pitz, C.K. Westbrook, A comprehensive modeling study of iso-octane oxidation, Combust. Flame 129 (3) (2002) 253–280.

[18] M. Mehl, W.J. Pitz, C.K. Westbrook, H.J. Curran, Kinetic modeling of gasoline surrogate components and mixtures under engine conditions, Proc. Combust. Inst. 33 (1) (2011) 193–200.

[19] X. You, F.N. Egolfopoulos, H. Wang, Detailed and simplified kinetic models of *n*-dodecane oxidation: the role of fuel cracking in aliphatic hydrocarbon combustion, Proc. Combust. Inst. 32 (1) (2009) 403–410.

[20] H. Wang, E. Dames, B. Sirjean, D.A. Sheen, R. Tangko, A. Violi, J.Y.W. Lai, F.N. Egolfopoulos, D.F. Davidson, R.K. Hanson, C.T. Bowman, C.K. Law, W. Tsang, N.P. Cernansky, D.L. Miller, R.P. Lindstedt, A high-temperature chemical kinetic model of *n*-alkane (up to *n*-dodecane), cyclohexane, and methyl-, ethyl-, *n*-propyl and *n*-butyl-cyclohexane oxidation at high temperatures, JetSurF version 2.0, <http://melchior.usc.edu/JetSurF/JetSurF2.0> (September 19 2010).

[21] S.S. Vasu, D.F. Davidson, Z. Hong, V. Vasudevan, R.K. Hanson, *n*-Dodecane oxidation at high-pressures: measurements of ignition delay times and OH concentration time-histories, Proc. Combust. Inst. 32 (1) (2009) 173–180.

[22] H.S. Shen, J. Steinberg, J. Vanderover, M.A. Oehlschlaeger, A shock tube study of the ignition of *n*-heptane, *n*-decane, *n*-dodecane, and *n*-tetradecane at elevated pressures, Energy Fuels 23 (5) (2009) 2482–2489.

[23] D.F. Davidson, D.R. Haylett, R.K. Hanson, Development of an aerosol shock tube for kinetic studies of low-vapor-pressure fuels, Combust. Flame 155 (1–2) (2008) 108–117.

[24] D.F. Davidson, Z. Hong, G.L. Pilla, A. Farooq, R.D. Cook, R.K. Hanson, Multi-species time history measurements during *n*-dodecane oxidation behind reflected shock waves, Proc. Combust. Inst. 33 (2011) 151–157.

[25] K. Kumar, G. Mittal, C.-J. Sung, Autoignition of *n*-decane under elevated pressure and low-to-intermediate temperature conditions, Combust. Flame 156 (6) (2009) 1278–1288.

[26] M.S. Kurman, R.H. Natelson, N.P. Cernansky, D.L. Miller, Speciation of reaction intermediates from *n*-dodecane oxidation in the low temperature regime, Proc. Combust. Inst. 33 (1) (2011) 159–166.

[27] P.S. Veloo, S. Jahangirian, F.L. Dryer, An experimental and kinetic modeling study of the two stage autoignition kinetic behavior of C_7, C_{10}, C_{12}, and C_{14} *n*-alkanes, in: Spring Technical Meeting, Central States Section of the Combustion Institute, April 22nd–24th, 2012.

[28] C. Ji, E. Dames, Y.L. Wang, H. Wang, F.N. Egolfopoulos, Propagation and extinction of premixed C_5 to C_{12} *n*-alkane flames, Combust. Flame 157 (2010) 277–287.

[29] A.P. Kelley, A.J. Smallbone, D.L. Zhu, C.K. Law, Laminar flame speeds of C_5 to C_8 *n*-alkanes at elevated pressures: experimental determination, fuel similarity, and stretch sensitivity, Proc. Combust. Inst. 33 (2011) 963–970.

[30] P. Pepiot-Desjardins, H. Pitsch, An efficient error propagation based reduction method for large chemical kinetic mechanisms, Combust. Flame 154 (2008) 67–81.

[31] P. Pepiot-Desjardins, H. Pitsch, An automatic chemical lumping method for the reduction of large chemical kinetic mechanisms, Combust. Theory. Mod. 12 (6) (2008) 1089–1108.

[32] S.S. Ahmed, F. Mauß, G. Moréac, T. Zeuch, A comprehensive and compact n-heptane oxidation model derived using chemical lumping, Phys. Chem. Chem. Phys. 9 (9) (2007) 1107–1126.

[33] P. Pepiot-Desjardins, Automatic strategies to model transportation fuel surrogates, Ph.D. thesis, Stanford University, Department of Mechanical Engineering, 2008.

[34] M.P. Burke, M. Chaos, Y. Ju, F.L. Dryer, S.J. Klippenstein, Comprehensive H_2/O_2 kinetic model for high-pressure combustion, Int. J. Chem. Kinet. 44 (7) (2012) 444–474.

[35] J. Troe, The thermal dissociation/recombination reaction of hydrogen peroxide $H_2O_2(+M) \leftrightarrow 2\,OH\,(+M)$ iii: analysis and representation of the temperature and pressure dependence over wide ranges, Combust. Flame 158 (4) (2011) 594–601.

[36] S. Sharma, S. Raman, W.H. Green, Intramolecular hydrogen migration in alkylperoxy and hydroperoxyalkylperoxy radicals: accurate treatment of hindered rotors, J. Phys. Chem. A 114 (18) (2010) 5689–5701.

[37] R. Asatryan, J.W. Bozzelli, Chain branching and termination in the low-temperature combustion of *n*-alkanes: 2-pentyl radical+O_2, isomerization and association of the second O_2, J. Phys. Chem. A 114 (29) (2010) 7693–7708.

[38] M. Cord, B. Sirjean, R. Fournet, A. Tomlin, M. Ruiz-Lopez, F. Battin-Leclerc, Improvement of the modeling of the low-temperature oxidation of *n*-butane: study of the primary reactions, J. Phys. Chem. A 116 (24) (2012) 6142–6158.

[39] H. Du, X. Gong, A theoretical study on the reaction mechanism of O_2 with C_4H_9 radical, J. Mol. Model. 18 (5) (2012) 2219–2226.

[40] W. Tsang, Chemical kinetic data base for combustion chemistry. Part 3: Propane J. Phys. Chem. Ref. Data 17 (2), 1988.

[41] H.-H. Carstensen, A.M. Dean, O. Deutschmann, Rate constants for the H abstraction from alkanes (RH) by radicals: a systematic study on the impact of R and R′, Proc. Combust. Inst. 31 (1) (2007) 149–157.

[42] J. Aguilera-Iparraguirre, H.J. Curran, W. Klopper, J.M. Simmie, Accurate benchmark calculation of the reaction barrier height for hydrogen abstraction by the hydroperoxyl radical from methane. implications for C_nH_{2n+2} where $n = 2$ to 4, J. Phys. Chem. A 112 (30) (2008) 7047–7054.

[43] T. Malewicki, K. Brezinsky, Experimental and modeling study on the pyrolysis and oxidation of *n*-decane and *n*-dodecane, Proc. Combust. Inst. 34 (1) (2013) 361–368.

[44] E. Olchanski, A. Burcat, Decane oxidation in a shock tube, Int. J. Chem. Kinet. 38 (12) (2006) 703–713.

[45] K. Kumar, C.-J. Sung, Laminar flame speeds and extinction limits of preheated *n*-decane/O_2/N_2 and *n*-dodecane/O_2/N_2 mixtures, Combust. Flame 151 (1) (2007) 209–224.

[46] X. Hui, C.-J. Sung, Laminar flames speeds of transportation-relevant hydrocarbons and jet fuels at elevated temperatures and pressures, Fuel 109 (2013) 191–200.

[47] H. Pitsch, M. Bollig, FlameMaster, a computer code for homogeneous and one-dimensional laminar flame calculations, Institut für Technische Mechanik, RWTH Aachen.

[48] D.B. Lenhert, The oxidation of JP-8 and its surrogates in the low and intermediate temperature regime, Ph.D. thesis, Drexel University, December 2004.

[49] C. Doute, J.-L. Delfau, R. Akrich, C. Vovelle, Chemical structure of atmospheric pressure premixed *n*-decane and kerosene flames, Combust. Sci. Technol. 105 (4–6) (1995) 327–344.

[50] D.C. Horning, D.F. Davidson, R.K. Hanson, Study of the high temperature autoignition of *n*-alkane/O_2/Ar mixtures, J. Prop. Power 18 (2) (2002) 363–371.

[51] A. Burcat, K. Scheller, A. Lifshitz, Shock-tube investigation of comparative ignition delay times for C_1–C_5 alkanes, Combust. Flame 16 (1) (1971) 29–33.

[52] J. Griffiths, P. Halford-Maw, D. Rose, Fundamental features of hydrocarbon autoignition in a rapid compression machine, Combust. Flame 95 (3) (1993) 291–306.

[53] A. Burcat, R.F. Farmer, R.A. Matula, Shock initiated ignition in heptane/O_2/argon mixtures, Proc. 13th Int. Symp. Shocks Waves (1981) 826–833.

[54] M.B. Colket, L.J. Spadaccini, Scramjets fuels autoignition study, J. Prop. Power 17 (2001) 315–323.

[55] H.K. Ciezki, G. Adomeit, Shock-tube investigation of self-ignition of *n*-heptane–air mixtures under engine relevant conditions, Combust. Flame 93 (4) (1993) 421–433.

[56] B.M. Gauthier, D.F. Davidson, R.K. Hanson, Shock tube determination of ignition delay times in full-blend and surrogate fuel mixtures, Combust. Flame 139 (4) (2004) 300–311.

[57] U. Pfahl, K. Fieweger, G. Adomeit, Self-ignition of diesel-relevant hydrocarbon–air mixtures under engine conditions, Symp. (Int.) Combust. 26 (1) (1996) 781–789.

[58] R. Minetti, M. Carlier, M. Ribaucour, E. Therssen, L.R. Sochet, A rapid compression machine investigation of oxidation and auto-ignition of *n*-heptane: measurements and modeling, Combust. Flame 102 (3) (1995) 298–309.

[59] N. Peters, G. Paczko, R. Seiser, K. Seshadri, Temperature cross-over and non-thermal runaway at two-stage ignition of *n*-heptane, Combust. Flame 128 (1) (2002) 38–59.

[60] V.P. Zhukov, V.A. Sechenov, A.Y. Starikovskii, Autoignition of *n*-decane at high pressure, Combust. Flame 153 (1) (2008) 130–136.

[61] E.W. Diau, M.C. Lin, C.F. Melius, A theoretical study of the $CH_3+C_2H_2$ reaction, J. Chem. Phys. 101 (1994) 3923–3927.

[62] S.G. Davis, C.K. Law, H. Wang, Propyne pyrolysis in a flow reactor: an experimental, RRKM, and detailed kinetic modeling study, J. Phys. Chem. A 103 (30) (1999) 5889–5899.

[63] P.A. Glaude, V. Conraud, R. Fournet, F. Battin-Leclerc, G.M. Côme, G. Scacchi, P. Dagaut, M. Cathonnet, Modeling the oxidation of mixtures of primary reference automobile fuels, Energy Fuels 16 (5) (2002) 1186–1195.

[64] S.G. Davis, An experimental and kinetic modeling study of the pyrolysis and oxidation of selected C_3 to C_8 hydrocarbons, Ph.D. thesis, Princeton University, Department of Mechanical and Aerospace Engineering, 1998.

[65] S.G. Davis, C.K. Law, Determination of and fuel structure effects on laminar flame speeds of C_1 to C_8 hydrocarbons, Combust. Sci. Technol. 140 (1–6) (1998) 427–449.